University of Cincinnati

Date: 9/9/2013

I, Megan L Lobaugh , hereby submit this original work as part of the requirements for the degree of Doctor of Philosophy in Nuclear & Radiological Engineering.

It is entitled:

Determination of Activity Deposited in the Axillary Lymph Nodes by Direct, In vivo Radiation Measurements

Student's name: **Megan L Lobaugh**

This work and its defense approved by:

Committee chair: Henry Spitz, Ph.D.

Committee member: Sam Glover, Ph.D.

Committee member: J. Kim, PhD

Committee member: Paul Succop, Ph.D.

6844

Determination of Activity Deposited in the Axillary Lymph Nodes by Direct, In vivo Radiation Measurements

A dissertation submitted to the
Graduate School
of the University of Cincinnati
in partial fulfillment of the
requirements for the degree of

Doctor of Philosophy

in the Nuclear and Radiological Engineering Program
of the College of Engineering and Applied Science
by

Megan L. Lobaugh

B.A., Miami University, 2006
M.S., University of Cincinnati, 2007

2013

Committee Chair: Henry B. Spitz, Ph.D.

ProQuest LLC.
789 East Eisenhower Parkway
P.O. Box 1346
Ann Arbor, MI 48106 - 1346

Abstract

This research improves the measurement of activity deposited in the axillary lymph nodes through the following specific aims:

A. *Determine the confounding influence of ^{241}Am deposited in organs adjacent to the axillary lymph nodes by simultaneous solution of the response functions for measurement of ^{241}Am deposited in the liver, lungs, and skeleton.*

Hypothesis: A series of direct, organ-specific measurements can be used to account for measurement interference for the axillary lymph nodes from activity deposited in other organs.

Radioactive material deposited in multiple organs of the body is likely to confound a result of an in vivo measurement performed over the lungs for routine occupational exposure monitoring. The significance of this interference was evaluated by measuring anthropometric torso phantoms containing lungs, liver, skeleton and axillary lymph nodes, each with a precisely known quantity of ^{241}Am uniformly distributed in the organs. Arrays of multiple high resolution germanium detectors were positioned over organs within the torso phantom containing ^{241}Am or over proximal organs without activity to determine the degree of measurement confounding due to photons emitted from other source organs. A set of four mathematical response functions describe the measured count rate with detectors positioned over each of the relevant organs and ^{241}Am contained in the measured organ or one of the other organs selected as a confounder. Simultaneous solution of these equations yields the activity deposited in each of the relevant organs. The matrix solutions described in this paper represent a technically valid method for adjusting a result of ^{241}Am measured in one organ for interferences that may arise from ^{241}Am deposited elsewhere, so internal dose from radioactive materials known to deposit in multiple organs may be evaluated based upon in vivo measurements.

B. Select the size and type of detector that offers the greatest sensitivity for ^{241}Am *in axillary lymph nodes measurements with the least measurement interference from* ^{241}*Am in other organs or tissue.*

Hypothesis: Detector selection can optimize sensitivity and decrease confounding for measurement of ^{241}Am deposited in the axillary lymph nodes.

The detection efficiency and interference susceptibility of four different types of low energy photon detectors, each with a unique geometric arrangement, were compared for direct measurement of ^{241}Am deposited in the axillary lymph nodes. Although the most efficient detector was a single large 23,226 mm^2 square phoswich detector, it was also the most susceptible to confounding from activity deposited in adjacent organs. The array of two 2,800 mm^2 high purity germanium detectors exhibited the highest efficiency per unit detector area with some resistance to confounding from activity deposited in the lungs. The array of two 4,560 mm^2 NaI(Tl) detectors was the least susceptible to confounding and nearly as efficient per square millimeter as the high purity germanium detector array. Selection of a detector system for measurement of activity deposited in the axillary lymph nodes should consider the likelihood for activity deposited in other organs, such as the lungs, to create an interference that will confound the measurement result.

Acknowledgements

This research was partially supported by:

- The National Institute for Occupational Safety and Health (NIOSH) University of Cincinnati Education and Research Center grant #T42/OH008432-10 and
- The Nuclear Forensics Graduate Fellowship Program, which is sponsored by the U.S. Department of Homeland Security, Domestic Nuclear Detection Office, and the U.S. Department of Defense, Defense Threat Reduction Agency, with additional support from the U. S. Department of Energy Nuclear Forensics Education Award Program at the University of Cincinnati.

Thank you to Dr. Henry Spitz and Dr. Samuel Glover for your continuing support and guidance. I appreciate your patience and willingness to let me pursue my career and life in California. Thanks to my committee for your thoughtful reviews. Dr. David Hickman you can stop bugging me now… thank you for your guidance, reviews, and motivators. Dr. John Hunt, obrigada por sua ajuda com VMC.

To all of my University of Cincinnati colleagues: thanks for the laughs, fun, and commiseration; I miss our times in the lab and office. To my LLNL colleagues: thanks for the motivation. To my friends: thanks for not rubbing it in (too much) when months turned into years.

And finally, Mom and Dad this is for you.

Table of Contents

Introduction

Workers who have the potential for internal exposure to radioactivity are routinely monitored for the presence of internal contamination using direct and indirect bioassay methods. Direct bioassay or in vivo measurement is a non-invasive technique for measuring photons emitted by activity deposited within the body. This includes whole body measurements, where detectors are positioned to measure radionuclides deposited in the entire body, and site-specific measurements, where radiation detectors are placed on or near the surface of the body over organs of interest.

Direct radiation measurements of internally deposited radioactive materials yield information about which nuclides are present and the quantity of activity deposited within the body. The gamma ray spectrum represents the number of photon interactions occurring within the detector and the energy of the photon(Knoll 2000). Each gamma-emitting radionuclide has a specific energy peak signature which is used to determine the identity of nuclides present in the body.

The activity of nuclides deposited within the body is determined by applying a factor which describes the efficiency (count recorded per photon emitted) of the detection system. Efficiency calibration factors are determined by measuring standards which contain a precisely known quantity of the nuclide and exhibit characteristics (e.g., shape, radiation attenuation properties) similar to the unknown material to be measured. Standards used for in vivo measurements simulate a radioactive material deposited within certain organs in the human thorax. The *de facto* standard adopted by the U.S. Department of Energy for in vivo measurement calibration is the Lawrence Livermore National Laboratory (LLNL) torso phantom (Snyder 2010).

The LLNL torso phantom was developed specifically to calibrate in vivo measurements for transuranic nuclides, whose emission energies are typically very low (i.e., less than 100keV). It is made from human tissue equivalent materials and was designed to represent the human torso from above the

hips to the neck, including removable organs in which radioactivity can be incorporated (Figure 1). Chest plates made of tissue equivalent material were designed to simulate attenuation of various chest wall thicknesses and body compositions (i.e., body fat percentages). Development criteria for the LLNL torso phantom included: reproducibility of measurement geometry for radionuclides deposited internally, simulation of low energy photon attenuation properties of human tissue, and ruggedness required for comparison measurements between various facilities (Griffith 1978). The LLNL torso phantom includes removable lungs, liver, heart, tracheobronchial lymph nodes, and gut. All of these tissues are fabricated using a formulation of polyurethanes which exhibit attenuation and density similar to human tissue. The UC LLNL torso phantom was modified to enable calibration measurements of the axillary lymph nodes, a network of lymph nodes in the axilla region, or armpit (Zeman 2009).

Direct measurements of the axillary lymph nodes are recommended following contaminated wounds on the hands or fingers, because the lymphatic system is the major route for removal of foreign bodies and particles that may be deposited in a wound. Radioactive particles deposited in a wound will migrate through the lymphatic system and deposit in the lymph nodes draining the wound site (Johnson 1970; Bistline 1972; Gomez 1972). Axillary lymph nodes drain wounds on the upper extremities, a common location for occupational injuries involving radioactivity. Since it is the most likely site for deposition following an upper extremity wound, it is also important to monitor the axillary lymph nodes because activity deposited there can interfere with routine lung monitoring. Activity deposited in the axillary lymph nodes which interferes with lung measurements can ultimately lead to erroneous assessment of occupational exposure (Zeman 2009).

The modification of the Livermore Torso phantom to include axillary lymph nodes gives a more realistic calibration technique for measurement of activity deposited in the axillary lymph nodes following wounds. To simulate the axillary lymph nodes, two parallel holes were drilled into the axilla region of the phantom and rods of muscle equivalent material with known quantities of Americium-241

sealed at one end can be inserted (Zeman 2009). The exact locations of the simulated axillary lymph nodes were determined from a computed tomography x-ray image of the modified phantom. The technical basis for and actual locations of the axillary lymph nodes in the modified phantom are described by Zeman (2009). The axillary lymph node phantom has been further improved by the development of new muscle equivalent overlays to simulate various attenuating thicknesses for the axilla region. These new overlays were required to obtain a linear regression model for efficiency across various thicknesses. A person's axilla region tissue thickness is determined via ultrasound or calculated via a regression model based on easily obtained biometric data. This thickness is then input into the radiation measurement efficiency calibration equation to yield a calibration factor. The calibration factor is applied to the unknown in vivo radiation measurement results to convert counts measured by the detector to the activity present in the axillary lymph nodes.

Anthropometric calibration standards, like the axillary lymph nodes phantom described, are used to relate in vivo radiation measurement results to the quantity of activity deposited in an organ or tissue. Activity results are then used to determine radiation dose, risk to the worker, and may be used to aid physicians in determining if medical remediation is required. Accurate efficiency calibration equations and factors for in vivo radiation measurements ensure accurate data for risk analysis and medical decisions.

This research improves efficiency calibration factors for in vivo radiation measurements of activity deposited in the axillary lymph nodes, by investigating the following specific aims:

A. *Specific Aim 1- Determine the confounding influence of ^{241}Am deposited in organs adjacent to the axillary lymph nodes by simultaneous solution of response functions for direct measurement of ^{241}Am deposited in the liver, lungs, and skeleton.*

Hypothesis: A series of direct, organ-specific measurements can be used to account for measurement interference for the axillary lymph nodes from activity deposited in other organs.

Inhaled or ingested radioactive materials will migrate and distribute in various organs and tissue based upon biokinetic and solubility characteristics of the material. Regardless of the route of intake, internally deposited radioactive material is likely to be distributed in more than one organ or tissue, complicating analysis of results obtained by in vivo monitoring. Contaminated wounds on a finger or hand represent another complication since a fraction of insoluble material is likely to phagocytize to one or more of the many lymph nodes located in axilla region of the upper thorax where activity may interfere with routine in vivo measurements of the lungs (NCRP 2007; Zeman et al. 2009). The conventional method for performing an in vivo measurement is to arrange the detector(s) over or around a specific location on the body so the solid angle of photons emitted from the activity deposition site subtends the maximum surface area of the detector entrance window. Unfortunately, unless adequately collimated or shielded, the detector may also respond to photons that enter the sensitive volume from other proximal organs or tissue in which activity is deposited (Palmer et al. 1983). Fisher and colleagues (2007), Zeman and colleagues (2009), and Carbaugh and colleagues (2010) have reported that activity deposited in the axillary lymph nodes creates an interference with routine lung counting.

Improperly assigning an activity deposition believed to be in one organ when it is actually due to activity in another organ or distributed in multiple organs can lead to an erroneous dose assessment (Sharma 1997). For example, following an accidental inhalation exposure to weapons-grade plutonium (i.e., a mixture that includes ^{241}Am) the activity will first deposit in the lungs and eventually a fraction will distribute to the liver and skeleton. Although a routine measurement of the lungs will likely detect activity, the result may erroneously be assigned solely to the lungs even though, especially for soluble forms of radioactive materials, the contribution from activity in the skeleton and liver may be quite significant. Improper assignment of activity leads to a biased estimate of radiation dose. Recognizing and

adjusting for measurement contributions from activity deposited in proximal organs helps to ensure accurate internal radiation dose estimates.

Neton (1988) described a mathematical calibration method for adjusting measurement results for confounding activity using matrix algebra and applied to activity deposited in the lungs, liver and thoracic skeleton. Since the axillary lymph nodes have been recognized as an important deposition site following contaminated wounds to the extremities and activity deposited within these lymph nodes has been shown to interfere with routine measures of the lungs, it is important to incorporate the axillary lymph nodes into a method for adjusting measurement results for confounding. Therefore, this specific aim extended Neton's mathematical calibration method to the axillary lymph nodes. Zeman and colleagues (2009) have described how the Livermore Torso Phantom was modified to accommodate axillary lymph nodes in the right and left shoulders. The matrix method considers organs in which activity is deposited as sources and organs which are the subject of in vivo measurement as targets. Target organs can also be source organs in the case of the typical direct calibration measurements. Application of this matrix method requires determination of contributions from all potential sources of photons in both source and target organs. These contributions are determined empirically from measurements of anthropometric calibration phantoms.

B. Specific Aim 2- Select the size and type of detector that offers the greatest sensitivity for ^{241}Am in axillary lymph nodes measurements with the least measurement interference from ^{241}Am in other organs or tissue.

Hypothesis: Detector selection can optimize sensitivity and decrease confounding for measurements of ^{241}Am deposited in the axillary lymph nodes.

Radioactive material deposited in a wound along the upper extremities of the body can be transported to the axillary lymph nodes where it may, in time, confound results obtained during routine

monitoring for inhaled radioactive material (Fisher et al. 2007). Therefore, workers who have incurred a contaminated wound on the arm, hand, or finger should be monitored for activity in the axillary lymph nodes to avoid the potential, at some future time, of incorrectly assigning to the lungs a deposition that is actually located in the axillary lymph nodes. Direct measurement of activity deposited in the axillary lymph nodes is a challenge, since radioactive material can be distributed among any one or more of the twenty to forty individual lymph nodes located around and under the pectoralis minor muscles of the upper torso (right or left shoulder). The Livermore Torso Phantom, which was originally designed as a calibration device for arrays of detectors used to measure activity deposited in the lungs, liver, and thoracic lymph nodes, was modified to include sources simulating activity deposited in the right or left axillary lymph nodes (Zeman et al. 2009). The conventional overlay plates supplied with the Livermore Torso Phantom, which provide a means to determine calibration factors for increasing thickness of the chest wall, do not extend over the shoulders under which the axillary lymph nodes are located. Therefore, a new set of extended overlay plates that cover the axilla region, as well as the anterior thorax, were fabricated so the change in detection efficiency with chest wall thickness could be determined for ^{241}Am in the axillary lymph nodes. The new overlay plates were fabricated using a formulation of polyurethanes that simulate human muscle (Griffith 1982).

Selecting an optimum type, number, and arrangement of detectors for measuring activity deposited in the axillary lymph nodes is challenging, because the distribution of activity in the axillary lymph nodes transported from a wound in a finger or hand is unpredictable, the thickness of overlying tissue in this part of the thorax is highly variable, and activity deposited elsewhere in the body may confound the measurement of activity in the axillary lymph nodes. Large surface area detectors are especially desirable when performing direct measurements of activity deposited in the body, since detection efficiency is directly proportional to the total surface area of the body covered by the detector. Historically, a pair of 12.7 cm or 15.24 cm diameter scintillation detectors was used to

measure activity deposited in the lungs. Arrays of multiple high-resolution germanium detectors, each with a surface area of 2,000-3,000 mm^2, are commonly used today for performing these measurements. A routine measurement of the lungs is likely to be confounded by activity deposited in the axillary lymph nodes because of their close proximity to the lungs. Likewise, in vivo measurement of the axillary lymph nodes will likely be confounded by activity present in the adjacent organs, such as lungs and bone.

Unfortunately, the location and arrangement of the network of axillary lymph nodes is highly variable from person to person, so predicting the distribution of activity deposited in the network is highly uncertain. Thus, a detector with a large surface area is conceptually more desirable than a small detector due to the improved likelihood that photons emitted by radioactive contamination will be detected efficiently with minimal geometric variation. Ideally the surface area of the detector should be sufficiently large so the solid angle of the detector encompasses all of the affected axillary lymph nodes. On the other hand, a large solid angle is likely to be susceptible to interference (i.e., confounding) from activity deposited in other nearby organs or tissue, especially the lungs. Therefore, determination of an optimal detector type and size for measuring activity in the axillary lymph nodes must incorporate the potential for confounding from activity deposited in the lungs.

This research investigated variations in detection efficiency related to detector type and tissue thickness when measuring ^{241}Am deposited in the right axillary lymph nodes. Also investigated was the potential that ^{241}Am deposited in the lungs would confound a measurement of ^{241}Am in the axillary lymph nodes. Since there is a potential for encountering these conditions when performing routine monitoring, this research investigated how detection efficiency and the potential for confounding are related to detector type and size.

Materials and Methods

All measurements were performed at the University of Cincinnati (UC) Nuclear and Radiological Engineering Program's Laboratory for In vivo Radiological Measurements. This facility is equipped with two graded-z shielded rooms, which provide shielding from background radiation and are typical of in vivo radiation measurements laboratories in industry and government facilities. Measurements were acquired and analyzed using Canberra Genie2k Gamma Acquisition and Analysis Software (Version 3.1a, May 2007). All anthropometric calibration phantoms used for this work were fabricated at UC using accepted formulations and procedures (Spitz et al. 1994; Spitz and Lodwick 2000). Each phantom has a precisely known activity of Americium-241 deposited. ^{241}Am was selected for this research since the low energy x-ray emissions with a high yield 59.5 keV gamma are considered an excellent analog for direct measurement of aged plutonium mixtures. Radiation decay information for Americium-241 is given in Table 1 (Browne 1986).

The University of Cincinnati LLNL Thoracic Phantom, modified to include axillary lymph nodes was used for all measurements. The original muscle equivalent overlays, which simulate attenuating thicknesses over the thorax, were used for measurements of the liver and lungs, because the attenuating thicknesses in these regions are well known. Chest wall thicknesses (CWT) for these overlays are given in Table 2. The original overlays for the Lawrence Livermore thoracic phantom were designed to simulate various known thicknesses of attenuating tissue overlying the organs of the thorax. When the UC LLNL Thoracic phantom was modified to include axillary lymph nodes, located in the axilla region of the torso phantom, the original overlays were deemed inadequate for this application.

New muscle equivalent overlay plates

The original overlays do not extend to completely cover the shoulders and axilla region of the phantom, where the cylindrical axillary lymph nodes sources are inserted. When using the original

overlays, attenuating tissue in the axilla region is lacking. The attenuating material doesn't extend to completely cover the measurement location for the axillary lymph nodes. The original overlays were not designed to be used for measurement in the axilla region and thus are inappropriate for this application. Knowing the precise thickness profile is important when determining an efficiency versus attenuating thickness calibration equation, therefore new overlays were developed.

Using standardized formulas and procedures for fabricating muscle tissue equivalent material, described previously by Spitz and Lodwick, seven new overlays (labeled A-1 through A-7) were fabricated to simulate attenuating thickness over the axillary lymph nodes (2000). Figure 2 shows the new overlays in position for measuring the axillary lymph nodes. The new overlays provide attenuating material in the axilla region and the chosen measurement geometry for the axillary lymph nodes.

The new overlays were measured for physical thickness, following similar procedures described previously (Robbins 2001). Using a micrometer gauge, thickness measurements were made at several points in a 1 centimeter by 1 centimeter grid over the detector measurement area of the axillary lymph nodes (Figure 3). Statistical tests reveal that the measured thickness (or log-transformed thickness) of the overlay plates is not normally (nor log-normally) distributed over the region covering the axillary lymph nodes. Therefore, the median value was adopted as the best estimate of tissue thickness for attenuation of photons emitted by ^{241}Am in the axillary lymph nodes. To establish the total tissue thickness, this median value for each new overlay is added to the average value of the two measured axillary lymph nodes' source depths in the phantom thorax base (Zeman et al. 2009). The physical thickness values for each overlay and the total tissue thickness values are given in Table 3. The total tissue thickness parameter is used to determine a regression model for the efficiency versus attenuating thickness calibration equation. Due to imperfections, A-1, A-2, and A-5 were chosen for measurement of the right axillary lymph nodes only. Overlays A-3, A-4, A-6, and A-7 can be used for measurement of either side.

A. *Specific Aim 1*

Determine the confounding influence of ^{241}Am deposited in organs adjacent to the axillary lymph nodes by simultaneous solution of response functions for measurement of ^{241}Am deposited in the liver, lungs, and skeleton.

A series of measurements was performed using specific arrangements of detectors over the Livermore Torso phantom with internal organs containing a precisely known quantity of ^{241}Am. Both the direct and indirect (i.e., interference) components of the photon radiation emitted by the organs and entering the sensitive volume of the detectors were evaluated. A detector response function was developed to describe the measured count rate for each unique arrangement of detectors and source organs. "Source" organs are those that contain ^{241}Am and contribute to the response of the detector. A source organ can also be the target organ, as in the case of the typical direct calibration measurements. "Targets" represent the specific organs being measured. Measurements are performed by arranging one or more detectors in a consistent, repeatable arrangement around the target organ. For example, activity deposited in the liver (source organ) may contribute to the lungs (target organ) when detectors are positioned over the lungs for a routine occupational exposure monitoring.

The detectors are arranged to measure target organ i. All photons entering and interacting within the sensitive volume of the detector are considered counts detected at target organ i. The total counts detected at organ i arise from (1) photons emitted from an isotope deposited in organ i plus (2) photons from isotopes deposited in other proximal organs. For example, the total counts detected at the lungs are the sum of photons originating from activity deposited in the axillary lymph nodes, skeleton, lungs, and liver. The count rate (counts per second) measured by the detector at target organ i is a function of the quantity of activity, Q, in each of the potential source organs:

$$cps_i = a_{i,lymph\ nodes}(x)Q_{LN} + a_{i,bone}(x)Q_{bone} + a_{i,lungs}(x)Q_{lungs} + a_{i,liver}(x)Q_{liver} \quad (1)$$

where the coefficients, $a_{i,j}$, of Q represent the efficiency of the detector (count per disintegration) located at target organ i for measuring activity emitted from each of the source organs, j. Expanding this response function to all four source organs yields a set of four equations describing the counts detected at each measured location:

$$
\begin{aligned}
cps_{LN} &= a_{LN,LN}(y)Q_{LN} + a_{LN,bone}(y)Q_{bone} + a_{LN,lungs}(y)Q_{lungs} + a_{LN,liver}(y)Q_{liver} \\
cps_{bone} &= a_{bone,LN}(x)Q_{LN} + a_{bone,bone}(x)Q_{bone} + a_{bone,lungs}(x)Q_{lungs} + a_{bone,liver}(x)Q_{liver} \\
cps_{lungs} &= a_{lungs,LN}(x)Q_{LN} + a_{lungs,bone}(x)Q_{bone} + a_{lungs,lungs}(x)Q_{lungs} + a_{lungs,liver}(x)Q_{liver} \\
cps_{liver} &= a_{liver,LN}(x)Q_{LN} + a_{liver,bone}(x)Q_{bone} + a_{liver,lungs}(x)Q_{lungs} + a_{liver,liver}(x)Q_{liver}
\end{aligned}
\tag{2}
$$

where $a_{i,j}(x)$ represents the efficiency for measurement with detectors arranged for target location i and activity deposited in source organ j at muscle equivalent chest wall thickness x or axillary lymph nodes muscle equivalent thickness y. Efficiency is measured as a function of the thickness of overlying tissue and is determined for each detector arrangement by applying increasingly thick layers of muscle tissue substitute on the surface of the Livermore Torso phantom containing organs with precisely known quantities of activity deposited uniformly throughout the tissue. These efficiency calibration equations convert measured counts to deposited activity. Simultaneous solution of these four equations yields the quantity, Q, of activity deposited in each source organ.

Matrix algebra can be used to solve the system of equations (2) from above:

$$
\begin{bmatrix}
a_{LN,LN}(y) & a_{LN,bone}(y) & a_{LN,lungs}(y) & a_{LN,liver}(y) \\
a_{bone,LN}(x) & a_{bone,bone}(x) & a_{bone,lungs}(x) & a_{bone,liver}(x) \\
a_{lungs,LN}(x) & a_{lungs,bone}(x) & a_{lungs,lungs}(x) & a_{lungs,liver}(x) \\
a_{liver,LN}(x) & a_{liver,bone}(x) & a_{liver,lungs}(x) & a_{liver,liver}(x)
\end{bmatrix}
\begin{bmatrix}
Q_{LN} \\ Q_{bone} \\ Q_{lungs} \\ Q_{liver}
\end{bmatrix}
=
\begin{bmatrix}
cps_{LN} \\ cps_{bone} \\ cps_{lungs} \\ cps_{liver}
\end{bmatrix}
\tag{3}
$$

where A is the matrix of calibration factors $a_{i,j}$ in terms of attenuating tissue thickness x or y, Q is the vector describing the activity deposited in each organ i, and cps_j is the measurement vector giving the measured counts per second at target organ j. The quantity, Q, of activity contained in each source organ can be determined by solving eqn (3) for Q:

$$\begin{bmatrix} Q_{LN} \\ Q_{bone} \\ Q_{lungs} \\ Q_{liver} \end{bmatrix} = \begin{bmatrix} a_{LN,LN}(y) & a_{LN,bone}(y) & a_{LN,lungs}(y) & a_{LN,liver}(y) \\ a_{bone,LN}(x) & a_{bone,bone}(x) & a_{bone,lungs}(x) & a_{bone,liver}(x) \\ a_{lungs,LN}(x) & a_{lungs,bone}(x) & a_{lungs,lungs}(x) & a_{lungs,liver}(x) \\ a_{liver,LN}(x) & a_{liver,bone}(x) & a_{liver,lungs}(x) & a_{liver,liver}(x) \end{bmatrix}^{-1} \begin{bmatrix} cps_{LN} \\ cps_{bone} \\ cps_{lungs} \\ cps_{liver} \end{bmatrix} \quad (4)$$

Populating the Calibration Matrix

Elements of the calibration matrix represent the detector response for each of the four target organ geometries when activity is deposited in one or more of the four source organs. The value of each of these matrix elements is determined by arranging detectors over each target organ and measuring photons from source organs containing precisely known quantities of radioactive material. The Livermore Torso Phantom is the consensus standard for calibrating detector systems used for in vivo measurement of radioactive materials deposited in the lungs, liver, or thoracic lymph nodes (Snyder 2010). Zeman and colleagues (2009) describe how the Livermore Torso Phantom used in this research was modified at the University of Cincinnati to include axillary lymph nodes. Lobaugh and colleagues (2012) describe fabrication of a set of seven new increasingly thick muscle equivalent overlay plates that extend over the axillary lymph nodes measurement position to determine the change in detector efficiency with tissue thickness which the original phantom overlays did not accommodate. The original overlay plates were used to determine efficiency for organs other than the axillary lymph nodes. The efficiency was measured using the Livermore Torso Phantom containing precisely known quantities of ^{241}Am in the liver, lungs, and axillary lymph nodes (Spitz et al. 1994; Spitz and Lodwick 2000; Zeman et al. 2009). A head phantom, fabricated at the University of Cincinnati by Kellar and colleagues (1995), containing ^{241}Am applied on the inner and outer surfaces of an imbedded skull was measured to determine activity in the skeleton. A thorax phantom fabricated at New York University (Cohen et al. 1984; Neton 1988) containing an imbedded skeleton labeled with ^{241}Am was used as a confounding source organ when measurements were performed over liver, lungs, and axillary lymph node target organs. Table 4 is a list of all phantom source organs used in this research. Americium-241 was selected

as the measured isotope since it emits low energy, high yield photons and is considered an analog for direct measurement of aged plutonium mixtures.

Arrays of the multiple high purity germanium (HPGe) detectors were used for this research; four detectors to measure the lungs and head, three detectors to measure the liver, and two detectors to measure axillary lymph nodes. Measurement data were acquired and analyzed using Canberra Genie2k Gamma Acquisition and Analysis Software (Version 3.1a, May 2007; Canberra Industries, Inc., 800 Research Parkway, Meriden, CT 06450, USA). Post measurement data analysis was performed using SAS (Version 9.3, 2010; SAS Institute Inc., 100 SAS Campus Drive, Cary, NC 27513-2414, USA) and MathCAD (Version 15, Parametric Technology Corporation Corporate Headquarters, 140 Kendrick Street, Needham, MA 02494, USA).

The diagonal elements of the calibration matrix are determined when the source organ is defined as the target organ. The efficiency of measuring low energy photons emitted by ^{241}Am in the lungs, liver, axillary lymph nodes, and thoracic skeleton is dependent upon the thickness of tissue between the detectors and the source organ. Therefore, a series of measurements of each source organ was performed using a set of increasingly thick overlay plates to determine the change in efficiency with tissue thickness. The plates were fabricated using a formulation of polyurethanes equivalent in radiation attenuation properties to muscle tissue. Eqn (5) was used to obtain the efficiency calibration factors for the target equals source organ arrangements for the lungs, liver, axillary lymph nodes, and thoracic skeleton:

$$Efficiency_{i,i}(x) = \frac{cps_{59.5keV,i}}{A_i} \quad (5)$$

where $cps_{59.5keV,i}$ is the count rate (counts s^{-1}) at 59.5keV measured with attenuating tissue thickness x, when detectors are arranged to measure source organ i and A_i is the activity (Bq) contained in source organ i. A linear regression model was used to determine measurement efficiency as a function of overlying muscle tissue thickness.

Off-diagonal elements of the calibration matrix represent the confounding contribution (i.e., interference or cross-talk) to a target organ measurement from activity deposited in another source organ. Cross-talk (source-to-target) measurement efficiencies are determined for each target organ position by inserting labeled source organs into the LLNL phantom torso cavity and positioning detectors over a designated target organ. Eqn (6) was used to determine the cross-talk efficiencies

$$Cross\text{-}Talk\ Efficiency_{i,j}(x) = \frac{cps_{59.5keV,i}}{A_j} \quad (6)$$

where $cps_{59.5keV,i}$ is the count rate (counts s^{-1}) at 59.5keV with attenuating tissue thickness x when detectors are positioned over target organ i and A_j is the activity (Bq) deposited in source organ j. Again, a series of measurements was made using a set of increasingly thick overlay plates to determine the change in measurement efficiency at target organ i due to activity deposited in source organ j. A linear regression of the measurement results across the attenuating tissue thicknesses yields an efficiency calibration equation for the interference response factor versus attenuating thicknesses. The matrix is populated with all the necessary calibration functions (Figure 4). All the target-to-source and target-to-target calibration equations for this research were calculated in a similar fashion, with a minor exception for the skeleton.

Activity deposited in the skeleton has the potential to significantly confound direct, in vivo measurements of most other target organs since the skeleton is widely distributed in the body and the deposition of activity in the skeleton varies based on many factors (e.g., different nuclides, type of bone, intake route, age at intake, etc.). For example, actinides, such as americium and plutonium, generally deposit on the surfaces of bone whereas alkaline earths, such as radium and strontium, generally deposit throughout the bone volume (ICRP 1967). The total deposition of activity in the skeleton is estimated by placing detectors around the head (skull) or knee and extrapolating the result to the total skeletal mass (Cohen et al. 1977). The head and knee are selected because their locations are least affected by activity deposition in other internal organs. UC has developed both anthropometric head

and knee calibration phantoms that contain ^{241}Am for this application (Kellar et al. 1995; Spitz and Lodwick 2000). In this research, the head phantom was used to determine the amount of activity deposited in bone. Efficiency calibrations for skull measurements are not a function of thickness, since the attenuating thickness covering the skull is relatively constant from person to person. Therefore, the mean of repeat measures was used as the efficiency calibration factor. Skull measurement results were normalized to the entire skeleton assuming Am-241 deposits on the bone surface areas. According to Neton (1988) the skull represents about 10.1% of the total skeletal surface area and this factor was chosen for extrapolation from measurement of the skull to total skeletal deposition.

Measurements of organs within the thorax may be susceptible to activity deposited within bones of the torso, so interference measurements were made with the thoracic skeleton phantom developed at New York University (Cohen et al. 1984; Neton 1988). It was fabricated from the thoracic skeleton of "an averaged-sized Caucasian male (estimated body weight = 150-155 lbs.) approximately 30 years old at death" (Neton 1988). The phantom contains a complete vertebral column, rib cage, scapulae, and clavicles. Activity was deposited on the inner surfaces by injecting ^{241}Am in uniformly distributed holes along all bones and was painted on the outer surfaces of all bones. Approximately, half of the activity was deposited within the inner surfaces of the bones and half was painted on the outer surfaces of the bones. The activity distribution within each of the bones was modeled after baboon data at 32 days post injection with ^{241}Am citrate. Tissue-equivalent lungs without activity deposited were included within the ribcage and the entire structure was embedded within muscle equivalent material (Cohen et al. 1984; Neton 1988). The interference response factors for the thoracic skeletal activity interference to the lungs, liver, and axillary lymph node measurements were normalized to total skeletal activity assuming Am-241 deposits on bone surface area. According to Neton (1988), the bones of the thorax represent about 28.4% of total skeletal surface area and this percentage was used to extrapolate the ribcage

activity to total skeletal deposition. Information for all phantoms used in this research are given in Table 4.

The change in efficiency with increasing tissue thickness for each of the matrix elements was evaluated using the PROC REG function in SAS. A second order polynomial was chosen to model the change in efficiency with the change in tissue attenuation and distance from the source. If the model fit was not significant using an F-statistic (α=0.10), the mean efficiency for that set of measurements was selected as the matrix entry. The complete matrix is populated with either functions describing the change in efficiency with increasing tissue thickness or means of repeat measures. The matrix is then applied to the results of an in vivo measurement to accommodate potential interferences (cross-talk) from depositions of activity in source organs proximal to the target organs being monitored.

The uncertainty for the calculated activity in any one organ is dependent on the activity in each of the other organs. The uncertainty of the measured count rate and efficiency calibration matrix were propagated through the matrix algebra performed to solve the system of linear equations, so an uncertainty for the calculated activity deposited in each organ could be reported. Root mean square error was assumed to represent the uncertainty of the linear regression matrix entries and standard deviation was assumed for the mean matrix entries.

The activity in one organ will increase the measurement background for all other organ measurements due to the cross-talk contributions. The measurement critical level is dependent on measurement background, so the contribution to measurement background from activity deposited in other organs was included in the calculation of the critical level (L_c). The minimum detectable activity (MDA) for this method was estimated by doubling the critical level as described by Currie (1967). Appendix A- Cramer's Rule illustrates the uncertainty propagation and critical level calculations.

Application of the Calibration Matrix

Application of the matrix method was demonstrated by evaluating four simulated measurements of the skull, lungs, liver, and axillary lymph nodes with the Livermore Torso phantom containing an undisclosed labeled organ. Table 5 lists the organs and undisclosed activity used in this "blinded" test. The overlying tissue thickness was limited to the basic phantom (i.e., 1.56 cm). The calibration matrix was inverted and multiplied by the measured count rate vector for the unknown deposition to determine the location and amount of activity deposited in each organ. Uncertainties for the calculated organ activities were determined by propagating the measurement uncertainties through the matrix algebra, as described in Appendix A- Cramer's Rule. These results were compared to the known amount of activity deposited in the organ phantom.

B. Specific Aim 2

Select the size and type of detector that offers the greatest sensitivity for ^{241}Am in axillary lymph nodes measurements with the least measurement interference from ^{241}Am in other organs or tissue.

An optimum detector for measurement of the axillary lymph nodes will exhibit a combination of good detection efficiency for 59.5 keV ^{241}Am photons with minimum interference from ^{241}Am deposited in other organs or tissue. Four different types and sizes of detectors, each designed for measuring low energy photons, were used in this study: (1) a pair of 4,560 mm^2 thin window NaI(Tl) scintillation detectors (Saint-Gobain 2005), (2) a 23,226 mm^2 square thin window NaI(Tl)/CsI(Tl) phoswich detector (Anderson and Kaifer 1982), (3) a 12,668 mm^2 thin window NaI(Tl) detector,[1] and (4) a pair of 2,800 mm^2 surface area high purity low energy germanium detectors (LEGe) (Canberra 2004). Table 6 lists the manufacturer's specifications for each detector used in this study. All the detectors have thin, low Z entrance windows. Measurements were performed using each detector arrangement with the right

[1] Email correspondence between Henry Spitz and Peter Menge (Saint Gobain) dated 2 September 2010.

axillary ^{241}Am lymph nodes inserted in the modified UC Livermore thorax phantom. The activity of ^{241}Am contained in the axillary lymph nodes and the lung phantoms is listed in Table 7. A set of efficiency versus tissue thickness calibration functions for each detector arrangement was obtained by performing a linear regression of the absolute detection efficiency (counts per gamma) measured at 59.5 keV using the new, increasingly thick overlay plates. The absolute efficiency of each detector arrangement was also calculated per unit surface area (counts per gamma-mm^2) defined as:

$$Efficiency\ per\ area = \frac{\frac{Counts_{59.5keV\ peak}}{Measurement\ Time\ (seconds)}}{Activity(Bq)_{axillary\ lymph\ nodes} \times Yield_{59.5keV} \times Detector\ Area(mm^2)} \quad (7)$$

where the activity is decay corrected to the date of measurement, and the yield data is from Ekstrom and Firestone (2009). An unattenuated ^{241}Am point source located on the face of the detector was used to normalize the absolute efficiency and the efficiency versus chest wall thickness. An average efficiency was determined to normalize detector arrays. Normalization of the response to a point source allows for the direct comparison of the different types of detectors, thus eliminating the effect of detector geometry on axillary lymph node efficiencies.

Contribution to the measurement of ^{241}Am in the axillary lymph nodes from activity deposited in the lungs was evaluated by inserting lungs containing ^{241}Am into the Livermore thoracic phantom and positioning each detector arrangement over axillary lymph nodes containing no ^{241}Am. Intuitively, the solid angle intercepted by larger detectors is more likely to be confounded by activity deposited in the lungs than smaller detectors. Measurements to evaluate confounding were performed using only the base plate on the phantom, since the solid angle is not significantly changed by increasing the thickness of the chest wall. The interference factor (from lung depositions) in units of counts per gamma is defined as:

$$Interference\ Factor = \frac{\frac{Counts_{59.5keV\ peak\ for\ axillary\ lymph\ nodes\ measurement}}{Measurement\ Time\ (seconds)}}{Activity(Bq)_{lungs} \times Yield_{59.5keV}} \quad (8)$$

Background measurements were made to investigate the figure of merit (FOM) and MDA for each detector arrangement. FOM is defined as:

$$\frac{1}{T} = \left(\frac{\sigma_s}{S}\right)^2 \frac{S^2}{(\sqrt{S+B} + \sqrt{B})^2}$$

where T is the total counting time to determine S, the counting rate due to the source without background; B is the counting rate due to background; and σ_s is the uncertainty of the source counting rate without background (Knoll 2000). This equation reduces to

$$\frac{1}{T} = \left(\frac{\sigma_s}{S}\right)^2 \frac{S^2}{4B}$$

for sources containing low activity when compared to background. FOM background count rates were determined with measurements of the Livermore Thoracic Phantom, while source count rates were determined from point source measures. Both FOM parameters were used in comparing the detectors. Background measurements of unexposed laboratory personnel were performed to determine the minimum detectable activity versus depth of axillary lymph nodes in the thorax using the phoswich detector and the germanium detector array. The depth of the axillary lymph nodes in the thorax for each person was estimated according to Bentel et al. (2000) and further employed for this application by Zeman et al. (2009):

$$x\ (cm) = \frac{1}{2}AP - 3$$

where AP is the anterior-posterior diameter at the axilla region and was measured for each person using a caliper.

Simulations of the confounding source-detector geometries were performed using Visual Monte Carlo (VMC Version 1.0, 2007; Instituto de Radioproteção e Dosimetria, Rio de Janeiro, RJ, Brazil), an application simulating particle transport within human tissue and human tissue substitutes. The high purity germanium detectors used at UC (manufactured by Canberra) were modeled for all simulated measurements. The UC owned LLNL torso phantom was modeled with appropriate volumes

representing relevant organs of interest, including the axillary lymph nodes. Activity was simulated in the axillary lymph nodes and lungs, so mathematical simulations could be compared to the measured values.

Results

A. Specific Aim 1

Seven of the sixteen efficiency calibration matrix entries were means of repeat measures, eight entries were regression equations, and one entry was zero ($1x10^{-15}$ was used for mathematical reasons). The final efficiency calibration matrix, A(x,y), is:

$$\begin{bmatrix} 0.00142y^2 - 0.0186y + 0.0640 & 4.05 \times 10^{-5} & 2.26 \times 10^{-5}y^2 - 3.35 \times 10^{-4}y + 0.00127 & -4.97 \times 10^{-7}y^2 - 5.06 \times 10^{-7}y + 2.28 \times 10^{-5} \\ 6.25 \times 10^{-5} & 6.95 \times 10^{-4} & 1.38 \times 10^{-6} & 1 \times 10^{-15} \\ 2.61 \times 10^{-4} & 3.65 \times 10^{-5}x^2 - 2.78 \times 10^{-4}x + 6.39 \times 10^{-4} & 2.30 \times 10^{-4}x^2 - 0.00261x + 0.00864 & -1.48 \times 10^{-5}x^2 - 5.29 \times 10^{-5}x + 8.31 \times 10^{-4} \\ -7.98 \times 10^{-7}x^2 - 2.976 \times 10^{-7}x + 3.98 \times 10^{-5} & 4.74 \times 10^{-6}x^2 - 3.73 \times 10^{-5}x + 1.01 \times 10^{-4} & 1.72 \times 10^{-4} & 4.30 \times 10^{-4}x^2 - 4.00 \times 10^{-3}x + 0.0113 \end{bmatrix}$$

where x is the chest wall thickness is centimeters and y is the axilla attenuating tissue thickness in centimeters. The uncertainty matrix is composed of the assumed uncertainties for each entry and was used in propagating uncertainties for the matrix method:

$$\sigma A = \begin{bmatrix} 1.7979 \times 10^{-4} & 9.605 \times 10^{-6} & 2.243 \times 10^{-5} & 9.040 \times 10^{-7} \\ 6.756 \times 10^{-8} & 6.984 \times 10^{-5} & 6.23 \times 10^{-7} & 1 \times 10^{-16} \\ 7.915 \times 10^{-5} & 2.229 \times 10^{-5} & 3.512 \times 10^{-5} & 2.396 \times 10^{-5} \\ 2.06 \times 10^{-6} & 3.12 \times 10^{-6} & 5.094 \times 10^{-5} & 1.417 \times 10^{-4} \end{bmatrix}$$

For the matrix entry which was a zero, an uncertainty of 10% was assumed for the uncertainty propagation. For matrix entries which were regression models, the root mean square error was used, making the uncertainty constant across the range of tissue thicknesses. For matrix entries which were means, the standard deviation was used.

Standard measurements of the axillary lymph nodes, skull, lungs, and liver were made with the undisclosed labeled organ in the Livermore Torso phantom at the core thickness to demonstrate application of the matrix method. Results (counts s^{-1}) for these demonstration measurements are given in the count rate vector:

$$cps = \begin{bmatrix} 5.39 \\ 0.171 \\ 59.4 \\ 3.81 \end{bmatrix} \begin{matrix} axillary\ lymph\ nodes \\ head \\ lungs \\ liver \end{matrix} .$$

The efficiency calibration matrix at the attenuating tissue thickness of the core phantom is:

$$A(1.56, 3.9) = \begin{bmatrix} 0.013 & 4.05 \times 10^{-5} & 3.07 \times 10^{-4} & 1.33 \times 10^{-5} \\ 6.25 \times 10^{-7} & 6.95 \times 10^{-4} & 1.38 \times 10^{-6} & 1 \times 10^{-15} \\ 2.61 \times 10^{-4} & 2.95 \times 10^{-4} & 5.13 \times 10^{-3} & 7.13 \times 10^{-4} \\ 3.74 \times 10^{-5} & 5.45 \times 10^{-5} & 1.72 \times 10^{-4} & 6.06 \times 10^{-3} \end{bmatrix}.$$

Multiplying the count rate vector by the inverse of the efficiency calibration matrix yields the vector of calculated activity (Bq) deposited in each organ. The calculated activity within the lungs is 17.77% higher than the known activity deposited within the phantom lungs used for the application measurement (Figure 5). The uncertainties for the calculated activities and critical levels (α=5%) for each measurement were calculated using the mathematical approach described in Appendix A- Cramer's Rule. The minimum detectable activity for this method and the application data was estimated by doubling L_c. Calculated activity, uncertainty, critical level, and MDA information are given in Table 8 and illustrated in Figure 6.

B. Specific Aim 2

Results of the measured efficiency and normalized efficiency for ^{241}Am in the axillary lymph nodes as a function of chest wall thickness establish the technical basis for comparing the performance of each detector arrangement. The large square phoswich detector exhibited the greatest efficiency at all axillary lymph node depths (Figure 7). On the other hand, the efficiency per unit detector surface area is greatest for the low energy germanium (LEGe) detector array (Figure 8). The absolute efficiency for each of the detector arrangements using a point source of ^{241}Am on the face of the detector is shown on Figure 9 (an average absolute efficiency is calculated for detector arrays). The square phoswich detector exhibits the greatest absolute point-source efficiency followed closely by the pair of NaI(Tl) scintillators and the array of high purity germanium detectors. Figure 10 shows the absolute efficiency for ^{241}Am in

the axillary lymph nodes for each detector arrangement normalized by the efficiency determined from measurement of the point source. The phoswich detector has the greatest normalized efficiency.

Figure 11 shows results of the expanded FOM and the low source rate simplification FOM for each of the detector arrangements. The round NaI(Tl) and phoswich detectors have the highest FOM (calculated with the expanded FOM equation and without regard to source rate), while the high purity germanium detector has the highest FOM for measurements of low activity sources. Figure 12 shows the minimum detectable activity versus axillary lymph node depth for the high purity germanium detector array and the phoswich detector. The MDA for the high purity germanium detector array is consistently lower than for the phoswich detector across the axillary lymph nodes depths investigated.

Measurements of interfering ^{241}Am activity in the lungs while the detectors were arranged over the axillary lymph nodes tended to confirm precepts associated with detector size. Figure 13 shows the interference efficiency as counts s^{-1} measured over the axillary lymph nodes per 59.5 keV gamma emitted from ^{241}Am in the lungs. The phoswich detector exhibited the greatest confounding from activity deposited in the lungs. The paired NaI(Tl) detector array had the least measurement confounding followed closely by the high purity germanium detector array. Since the high purity germanium detector array had the highest FOM for low activity measurements, lowest minimum detectable activity at all depths of the axillary lymph nodes investigated (3 cm to 6 cm), and low interference from activity deposited in the lungs, it is the best overall detector for exposure monitoring of the axillary lymph nodes.

Figure 14 is an illustration of a VMC simulation of the UC LLNL torso phantom. The UC HPGe detectors were modeled and positioned in the typical lymph nodes and lungs geometries. Results for the simulations are given in Table 9. The simulations didn't agree as well as originally thought. Simulation of measurement of the right axillary lymph nodes with activity deposited in the axillary lymph nodes was 66% different from the measurement data. Simulation results of the interference to the axillary lymph

nodes measurement from activity deposited in the lungs was 148% different. Simulation results of the interference of lungs measurements from activity deposited in the axillary lymph nodes was 63% different.

Discussion

A. Specific Aim 1

Direct, in vivo measurement of ^{241}Am deposited in the lungs presents special challenges since the 59.5keV photons are significantly attenuated by overlying tissue and thoracic skeleton between the source organs and detectors. Therefore, it is important to evaluate how the tissue thickness affects detection efficiency. Each element of the calibration matrix was measured using increasingly thick overlay plates that fit snugly over the base of the Livermore Torso Phantom to reveal how efficiency changes with chest wall thickness. As with all statistical models, these are only valid within the range of data used to develop them; extrapolation beyond the attenuating thicknesses represented by the new overlays must be done with caution (Table 10).

Unfortunately, the overlay plates did not fit as well on the NYU thorax phantom containing the labeled skeleton and may have introduced some additional uncertainty in the matrix elements involving bone and axillary lymph nodes. This uncertainty isn't thought to be any larger than typical sources of uncertainty for in vivo measurements (e.g., detector placement variability, biological variability, etc.). The overlays for the axillary lymph nodes measurement were designed to simulate up to 6.67 cm of attenuating thickness. When the interference measurements were made with the lungs and liver confounding, it was found that the thickest overlay forced the detectors to be positioned in such a way that photons were streaming through the seams of the LLNL Torso phantom causing an unexpected increase in efficiency at this thickness. Therefore, the 6.67 cm overlay was not used for these interference measurements making the largest simulated thickness 5.16 cm.

The matrix efficiency calibration equations for the lungs and liver measurement geometries had probabilities of the F-statistic summed with the R-squared equaled one. This was due to the calculation of the probability of the F-statistic for two degrees of freedom reducing to the calculation of the R-squared. See Appendix B. R-squared and Probability of the F-test Statistic Sum for a more detailed explanation. The significance of the quadratic model for the liver as target organ and the lungs as source organ was rejected at the α=0.10 level. This outcome is likely due to the position and size of the liver and lungs relative to the small surface area of the detectors enabling unscattered photons to enter the detectors from a wide solid angle, so changes in efficiency with tissue thickness becomes relatively constant. The skull measurement with the liver as source organ was the only zero matrix entry. The 59.5keV peak was not identified by the Genie2k Gamma Acquisition and Analysis software and the region of interest displayed counts equal to the skull background measurement. This may cause problems for calculation of the activity vector. The distance from the liver to the head and very small solid angle for the source to target is likely causing the low count rate for this measurement. The low count rate in this geometry supports the decision to use of head measurements for determining total skeletal activity, because there is very low cross-talk interference.

The choice of normalizing factors for extrapolating skull measurements to total skeletal deposition is a challenge given the many variables affecting skeletal deposition. The exact deposition location within the bone (surface vs. volume seekers), time post exposure, as well as trabecular and cortical bone content of the measured area compared to the total skeleton, must be considered when choosing the factor for extrapolating measurement data to total skeletal deposition. For example, the skull is 95% cortical bone, while the rest of the skeleton is mostly made of trabecular bone (ICRP 2002). Percentage of total skeletal surface area was chosen as the normalizing factor in this application because americium and plutonium deposit on bone surface areas (ICRP 1967). The bone surface area percentages used as

the normalizing factors for this application were calculated by Neton and agree well with the mean Am-241 percentages of skeletal activities published later by Lynch and colleagues (1988).

The application of the matrix calibration example uses measures of the UC LLNL thorax phantom with the deposition location and quantity blinded to the detector operator. The results of this application yielded a correct deposition location and the amount of activity was within the typical range of percent differences for in vivo measurements (Jeffers and Hickman 2012). Calculated activities for the proximal organs without activity deposited were non-zero numbers, but the calculated lymph nodes activity and liver activity were close to the MDA for the method. The skeletal activity was much higher than the MDA and non-zero. The very low critical level for the skeletal activity deposition calculation and MDA is likely due to the zero entry for the liver contribution to the skull measurement.

Especially when making routine in vivo measurements for occupational exposure monitoring this mathematical system needs to be able to detect new intakes. The critical level and MDA were calculated assuming not only the measurement background for a typical measurement, but also assuming an increase in background due to interferences from activity deposited in each of the other proximal organs. This represents a more realistic measurement critical level. One drawback to the data presented here is that it is for phantom backgrounds and not using human background data. An improvement would be to use this approach with data from a population of workers unexposed to weapons grade plutonium or americium to determine a background versus attenuating tissue thickness equation for the critical level calculations.

B. Specific Aim 2

This investigation shows that the larger surface area detectors exhibit the greatest efficiency for detecting ^{241}Am deposited in the axillary lymph nodes, but these same detectors yield a more confounded result when activity is present in the lungs. Therefore, measurements of axillary lymph nodes in persons having no other internal deposition of radioactive material in adjacent tissues or

organs can be accurately and reliably performed using detectors with a large surface area. Smaller surface area detectors should be used for in vivo measurement of the axillary lymph nodes for persons known to have other internal deposition in nearby tissues or organs to minimize confounding. Fisher et al. (2007) have shown that activity deposited in the axillary lymph nodes will confound a routine in vivo measurement of the lungs. Thus, it is important to determine whether the person being monitored has ever incurred an internal deposition of activity in upper torso organs and tissues or in the upper extremities to avoid errors in lung dose assessment. This study was limited to evaluation of ^{241}Am in the axillary lymph nodes and lungs. The use of a high-resolution germanium detector array may be preferred if unknown or multiple radionuclides are present, since isotope identification specificity is better for solid-state than scintillation detectors. Unlike solid-state detectors, scintillation detectors are very sensitive to effects of spectral degradation and effective peak shifting, which arise as the chest wall thickness increases. Although manual adjustment of regions of interest in the measured spectrum can alleviate some of this problem, spectral degradation leads to greater uncertainty in the measured result. Figure 15 shows the effect of spectral degradation at the shallowest axillary lymph node depth (base thickness = 3.85 cm). Degradation and effective peak shift increases were observed in this study with increasing tissue thickness.

The FOM calculated to compare these detectors represents the inverse of the total counting time needed to attain the desired precision when a time, T, is available to measure signal in the presence of background and background alone. In vivo monitoring involves low source rate measurements in a comparatively high background; therefore, the low activity FOM is most pertinent in this application. The minimum detectable activity (MDA) is also important because it reveals the sensitivity of the technique for monitoring occupational exposures.

The VMC simulation of the axillary lymph nodes measurement with activity deposited in the axillary lymph nodes was half the measured value. This difference can be attributed to activity being

deposited in both the right and left axillary lymph nodes in the simulation, while for the measurements the activity was only deposited in the right axillary lymph nodes. When the calibration factor was calculated via the VMC program the entire activity was divided by the detector count rate. This could not be manipulated by the user and is a drawback to this software, because in reality when a worker sustains an injury only one side of the lymph nodes would be affected, not both. Other differences between the VMC simulations and measured values weren't as large and are likely due to the fact that the angle of the detectors could not be manipulated in VMC. In vivo measurement results are highly susceptible to changes in detector geometry. In the program detector angle can be manipulated, but the author of the program warned against using this feature, since it is still being improved.

Conclusion

Radioactive material deposited in multiple organs of the body is likely to confound results of routine in vivo monitoring performed over the lungs. The matrix solutions described in this paper represent a method for adjusting a result of ^{241}Am directly measured in one organ for interferences that may arise from ^{241}Am deposited elsewhere. This method represents a technically valid method to aid in evaluating internal dose based upon in vivo measurements for those radioactive materials known to deposit in multiple organs.

Results of the axillary lymph nodes detector comparison confirm the precept that the larger square phoswich detector has the highest absolute efficiency. However, detectors having a large surface area also exhibited the greatest potential for confounding, since the solid angle associated with the large detector overlaps the lung region. In terms of basic detection, the array of high purity germanium detectors is better than the large phoswich detector. The high purity germanium detector array exhibited the highest absolute efficiency per unit area followed closely by the array of two 4,560 mm^2 NaI(Tl) detectors. Both germanium and thin, small diameter scintillators were equally efficient in

measuring ^{241}Am in the axillary lymph nodes of the phantom. The high purity germanium detector array had the highest FOM for low activity measurements and the lowest minimum detectable activity for all depths of axillary lymph nodes. Therefore, of the four detectors investigated, the high purity germanium detector is the best choice for axillary lymph node measurements.

Figures

Figure 1. Lawrence Livermore Torso Phantom used for calibration of direct, in vivo radiation detection systems.

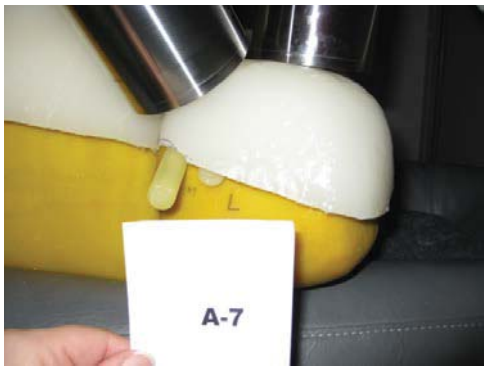

Figure 2. High resolution germanium detectors positioned for measurement of the right axillary lymph nodes on the Livermore thoracic phantom covered by one of the new overlay plates. Two cylindrical rods of muscle tissue substitute representing axillary lymph nodes containing ^{241}Am can be seen protruding from the shoulder of the Livermore thoracic phantom.

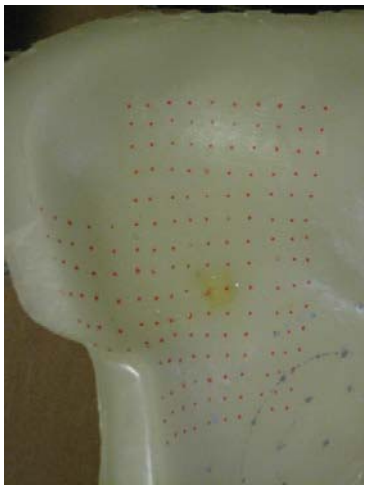

Figure 3. Posterior surface of a new overlay plate showing the 1 cm by 1 cm grid of points (red dots) at the shoulder where tissue thickness was measured.

Measurement geometry (target organ)	*Organ with radioactivity deposition (source organ)*			
	Axillary Lymph Nodes	Skeleton	Lungs	Liver
Axillary Lymph Nodes	$a_{LN,LN}(y)$	$a_{LN,\ skeleton}(y)$	$a_{LN,\ lungs}(y)$	$a_{LN,liver}(y)$
Skull	$a_{skull,\ LN}(x)$	$a_{skull,\ skeleton}(x)$	$a_{skull,\ lungs}(x)$	$a_{skull,\ liver}(x)$
Lungs	$a_{lungs,\ LN}(x)$	$a_{lungs,\ skeleton}(x)$	$a_{lungs,\ lungs}(x)$	$a_{lungs,\ liver}(x)$
Liver	$a_{liver,\ LN}(x)$	$a_{liver,\ skeleton}(x)$	$a_{liver,\ lungs}(x)$	$a_{liver,\ liver}(x)$

Figure 4. Calibration matrix where the diagonal terms are the typical efficiency calibration equations and off-diagonal terms are the interference response equations. Each entry is an equation representing the calibration factor as a function of attenuating tissue thickness: x as chest wall thickness and y as thickness in the axillary lymph node region.

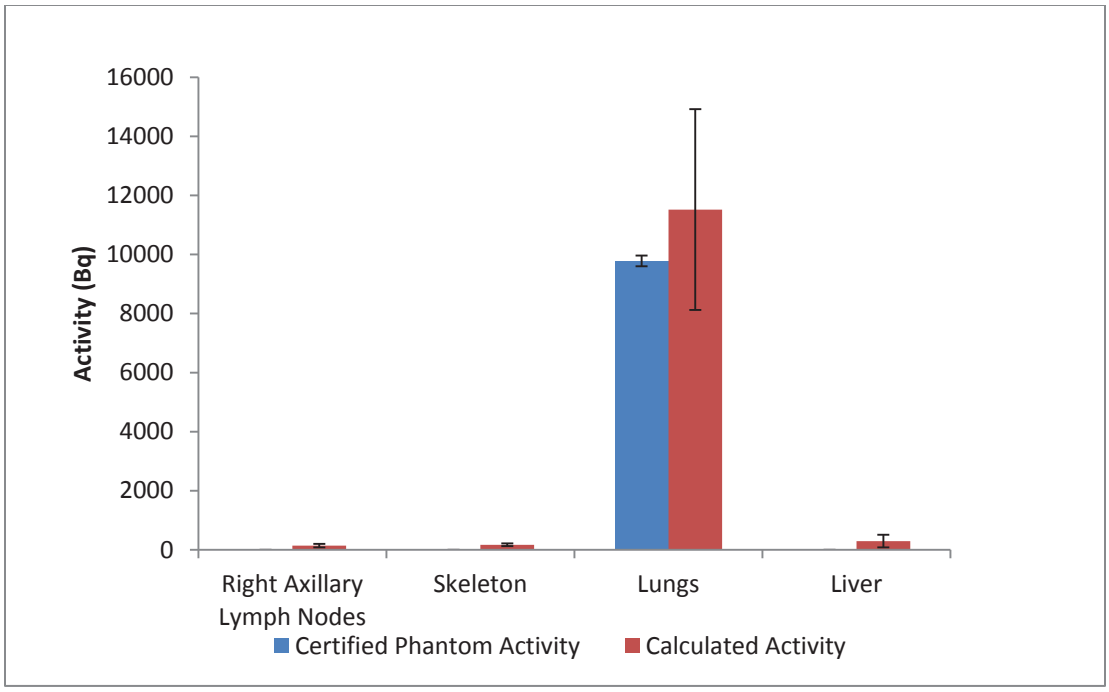

Figure 5. Comparison of matrix method calculated activity versus the anthropometric organ phantom certified activity in Bq. Uncertainty bars represent 2σ.

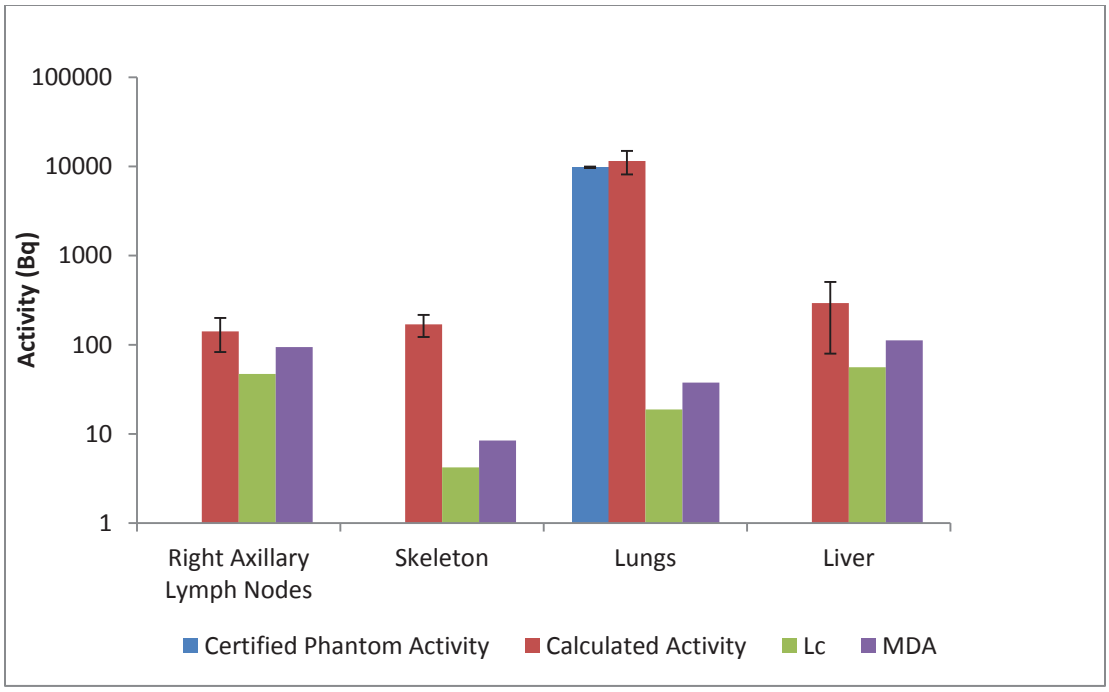

Figure 6. Comparison of the calculated activity for measurement locations without activity present to the critical level and minimum detectable activity.

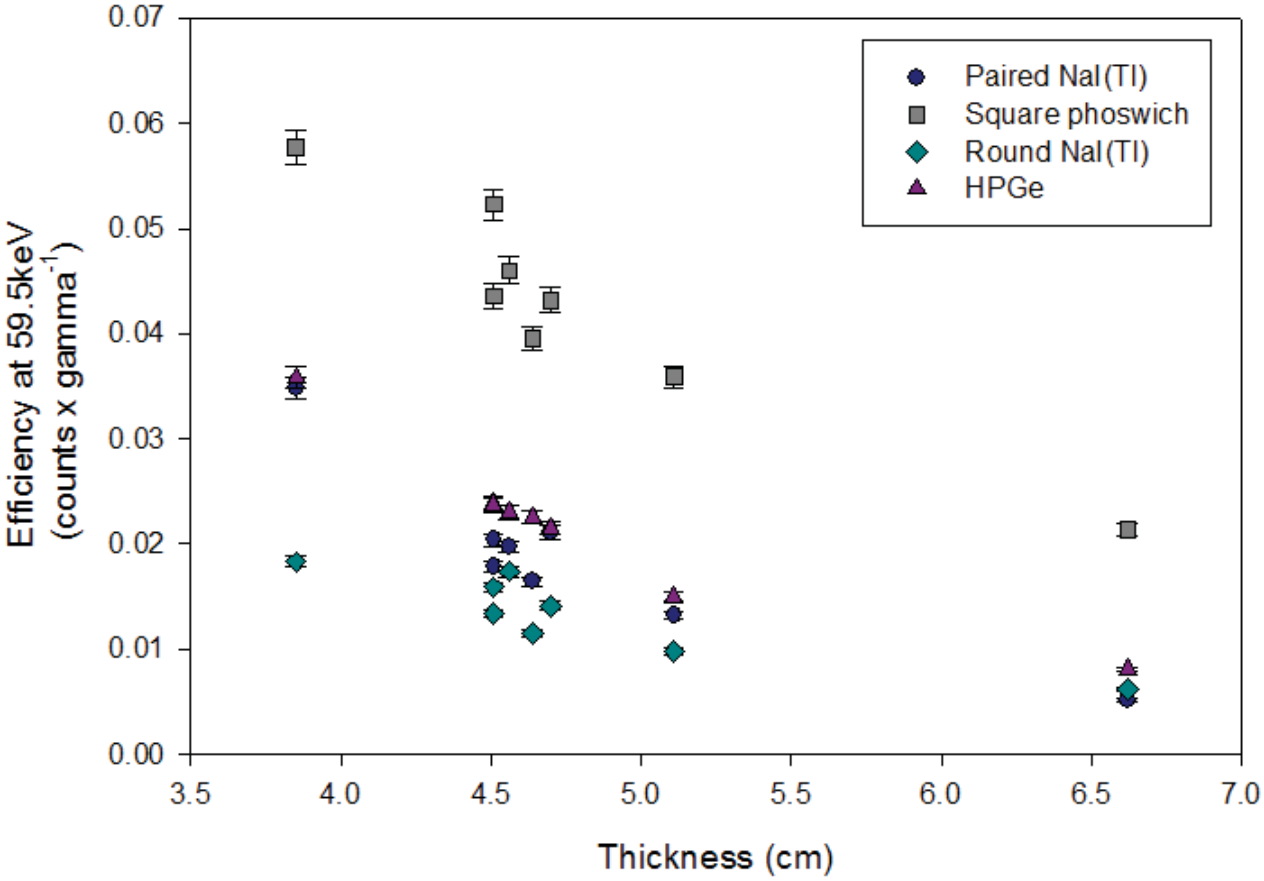

Figure 7. Detector comparison based on efficiency versus attenuating tissue thickness. Each detector made similar measures of the right axillary lymph nodes phantom across the eight attenuating tissue thickness represented by the base and seven new overlays. Error bars represent two times the propagated measurement uncertainty.

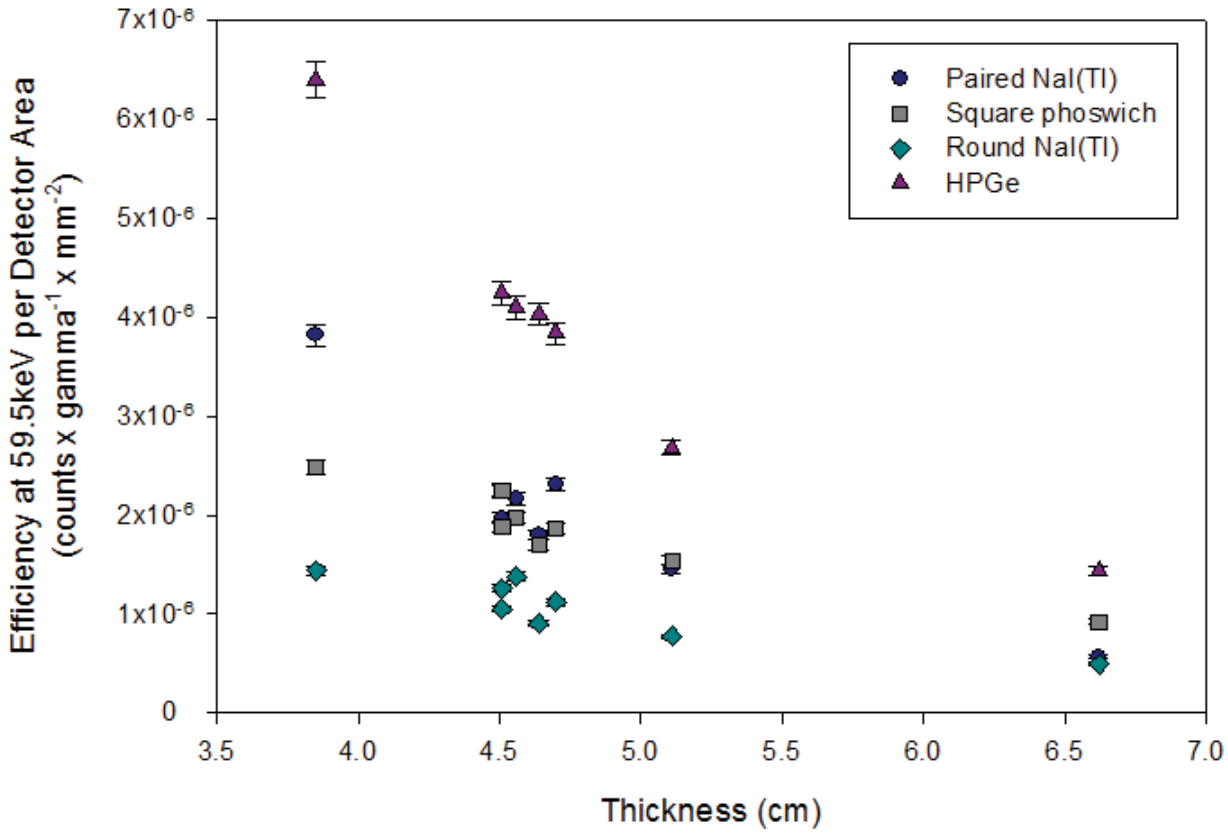

Figure 8. Comparison based on detector area-normalized efficiency measures. Efficiency versus attenuating tissue thickness measures were normalized by the detector area from the manufacturer's specifications (Table 6). Error bars represent two times the propagated measurement uncertainty.

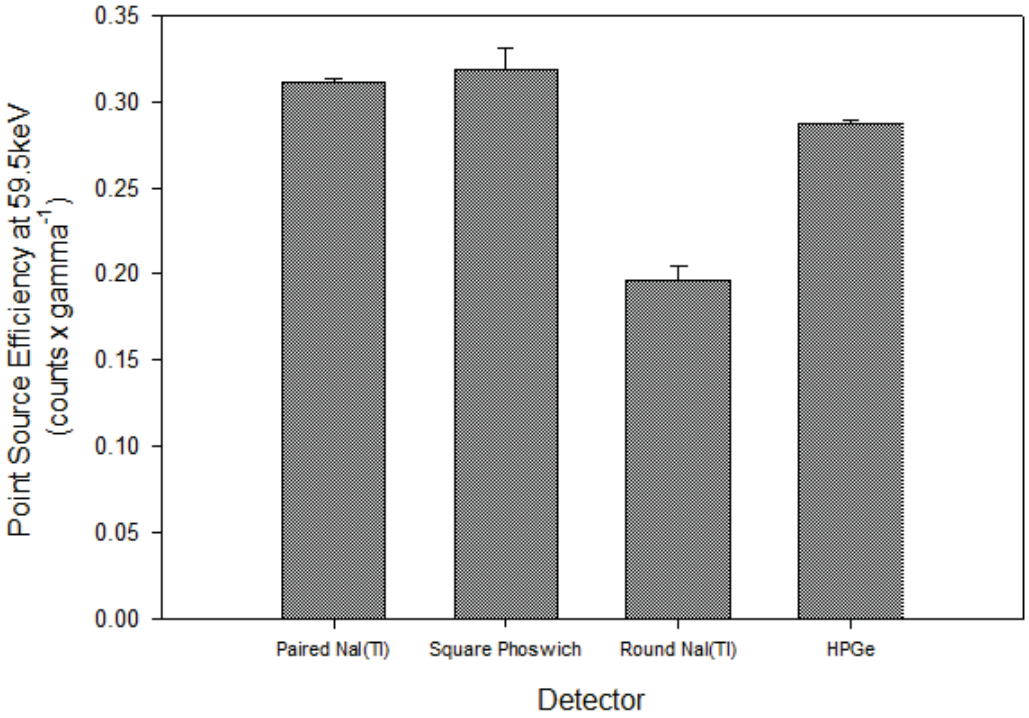

Figure 9. Point source efficiency for each detector. Error bars represent two times the propagated measurement uncertainty.

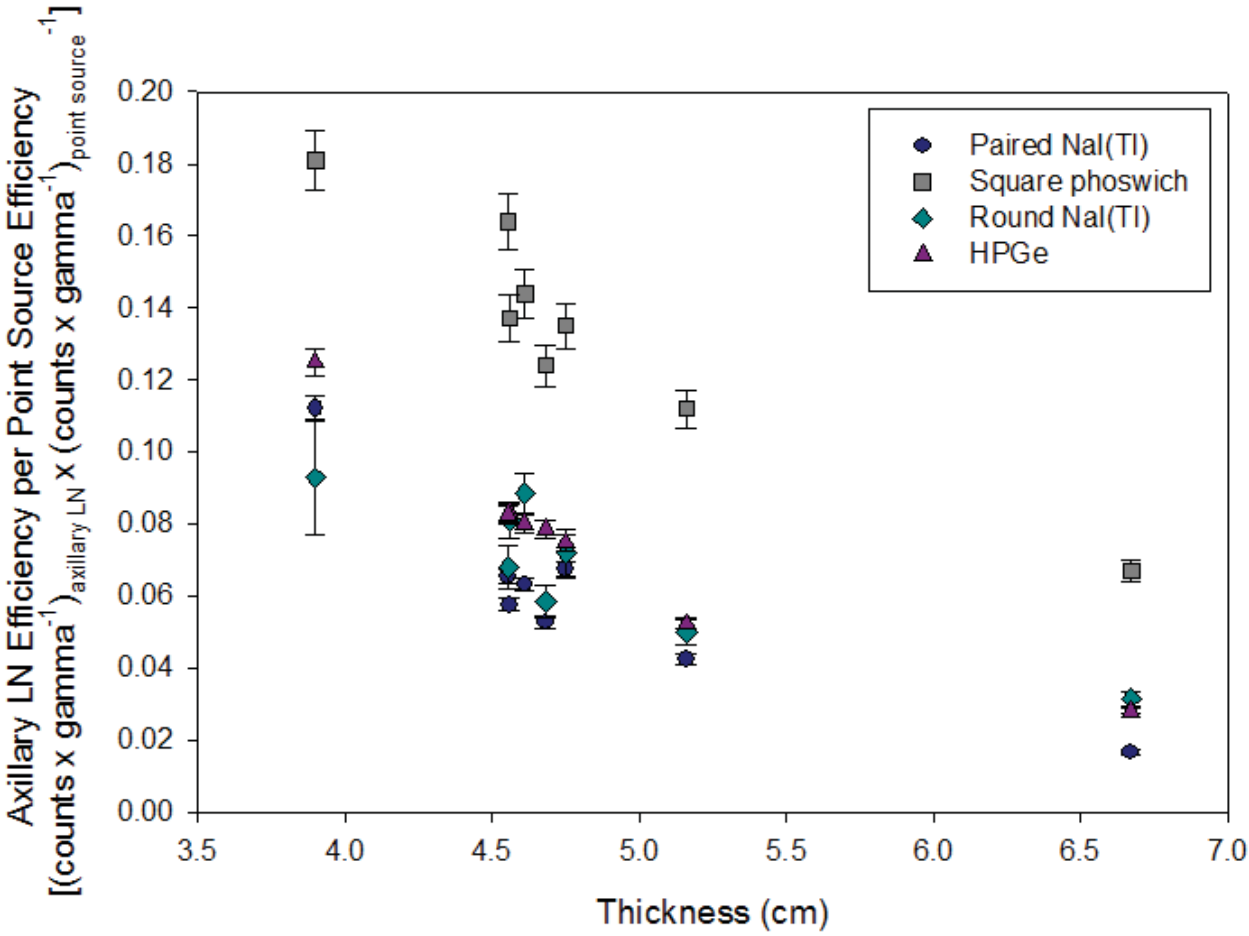

Figure 10. Comparing the four detectors based on efficiency per point source efficiency for various attenuating tissue thicknesses. Each detector measured a point source near the face and absolute efficiency was calculated. The efficiency versus attenuating tissue thickness calculations were normalized to this point source efficiency. Error bars represent two times the measurement uncertainty.

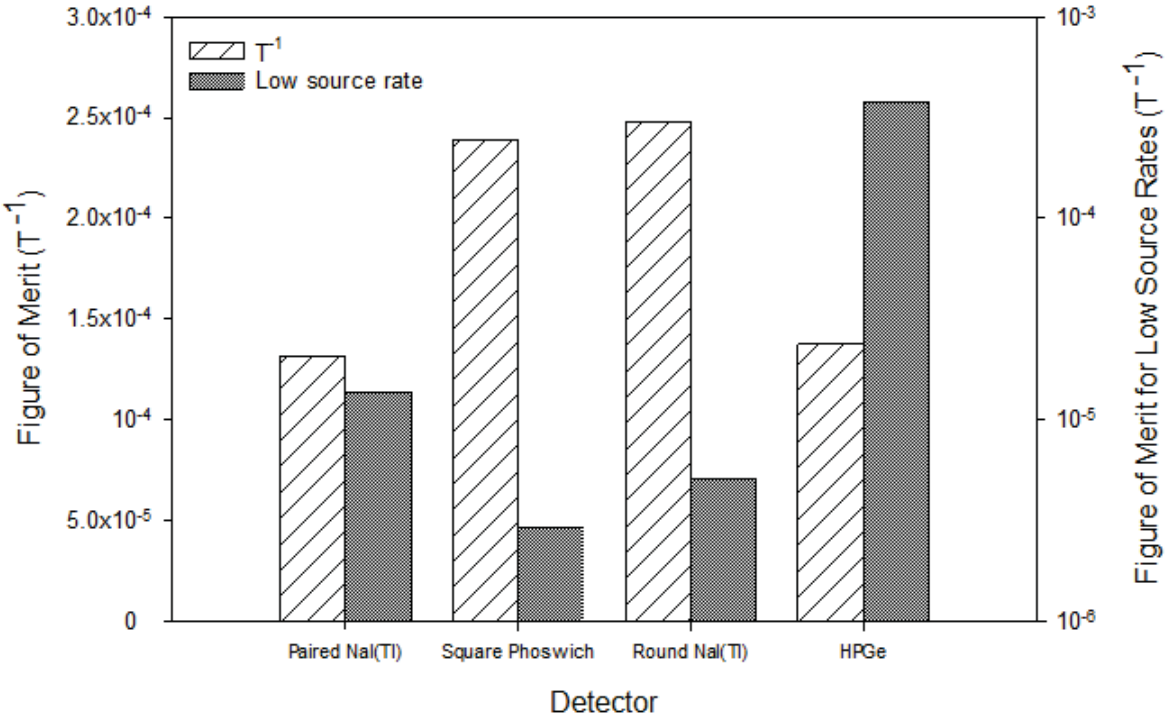

Figure 11. Figure of Merit, including the low source rate simplification.

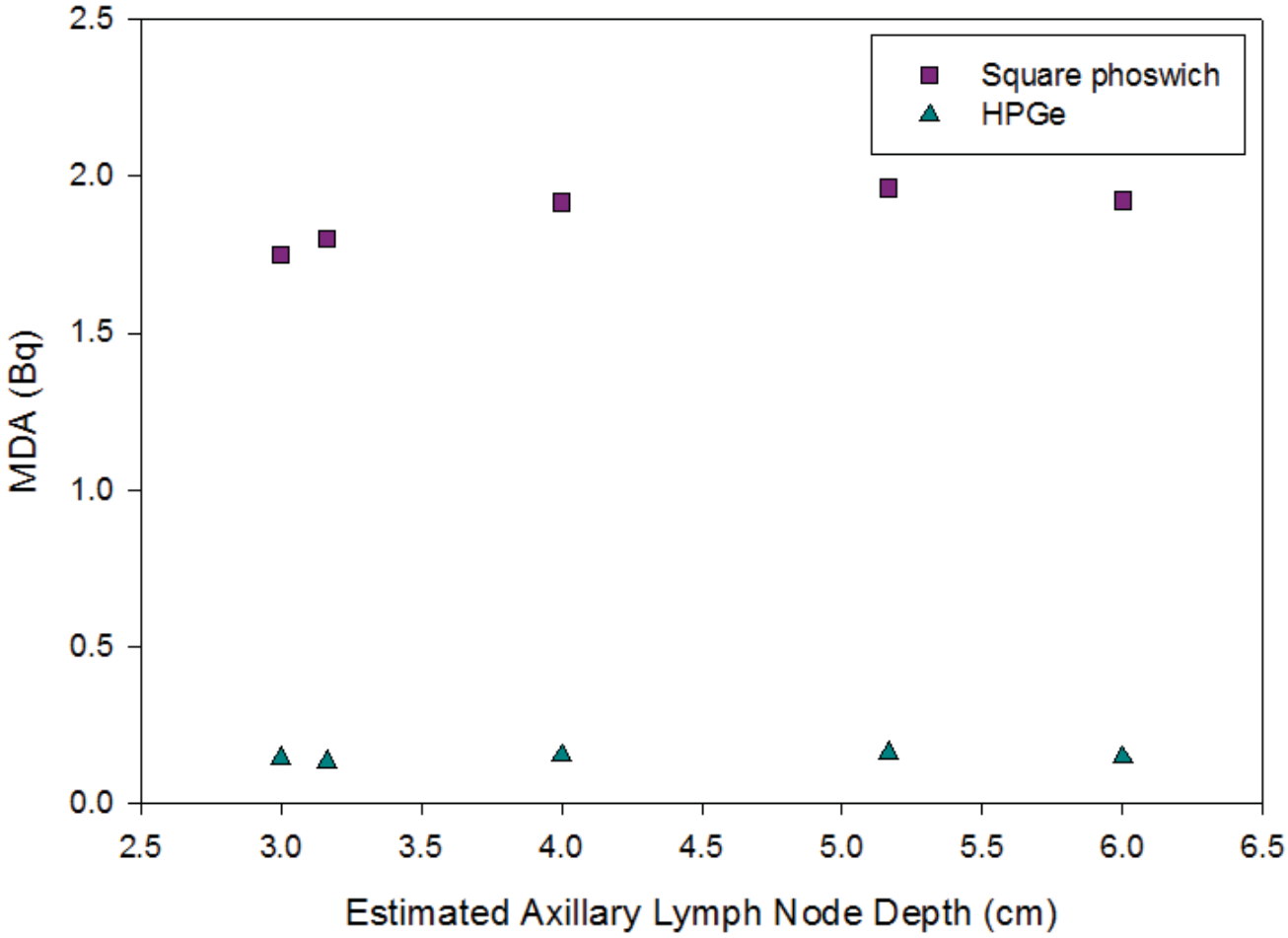

Figure 12. Minimum detectable activity calculated for the square phoswich and high purity germanium detectors as a function of axillary lymph node depth.

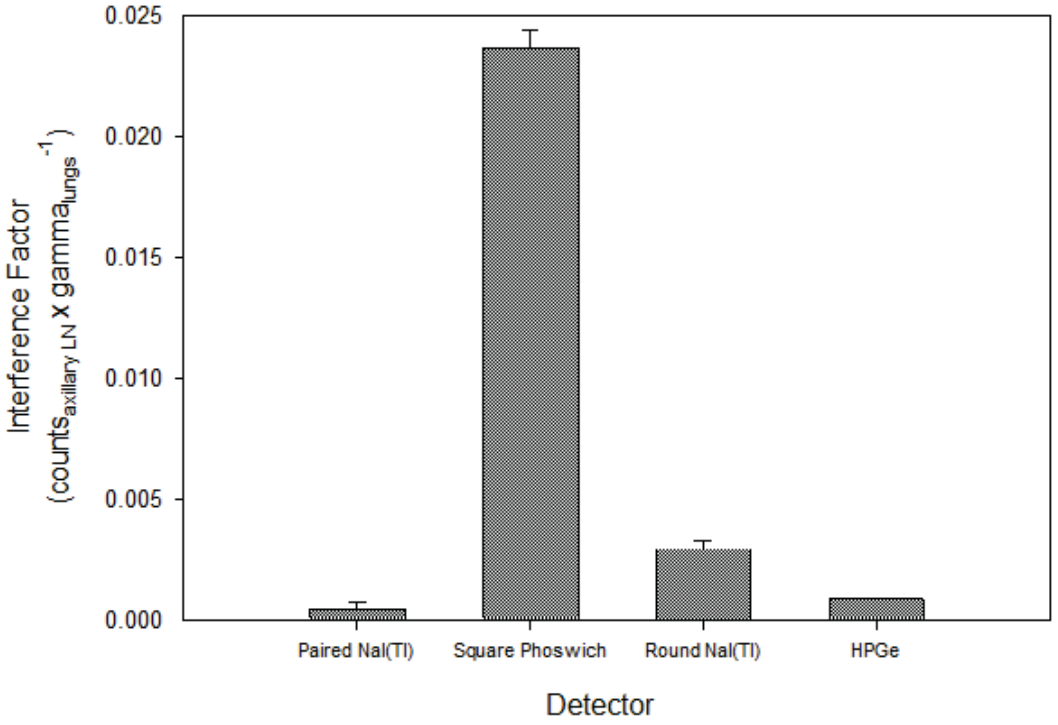

Figure 13. Comparing the four detectors based on the interference from activity deposited in the lungs. The interference factor represents the cps detected at the axillary lymph nodes per gamma emitted from the lungs phantom. Error bars represent two times the propagated measurement uncertainty.

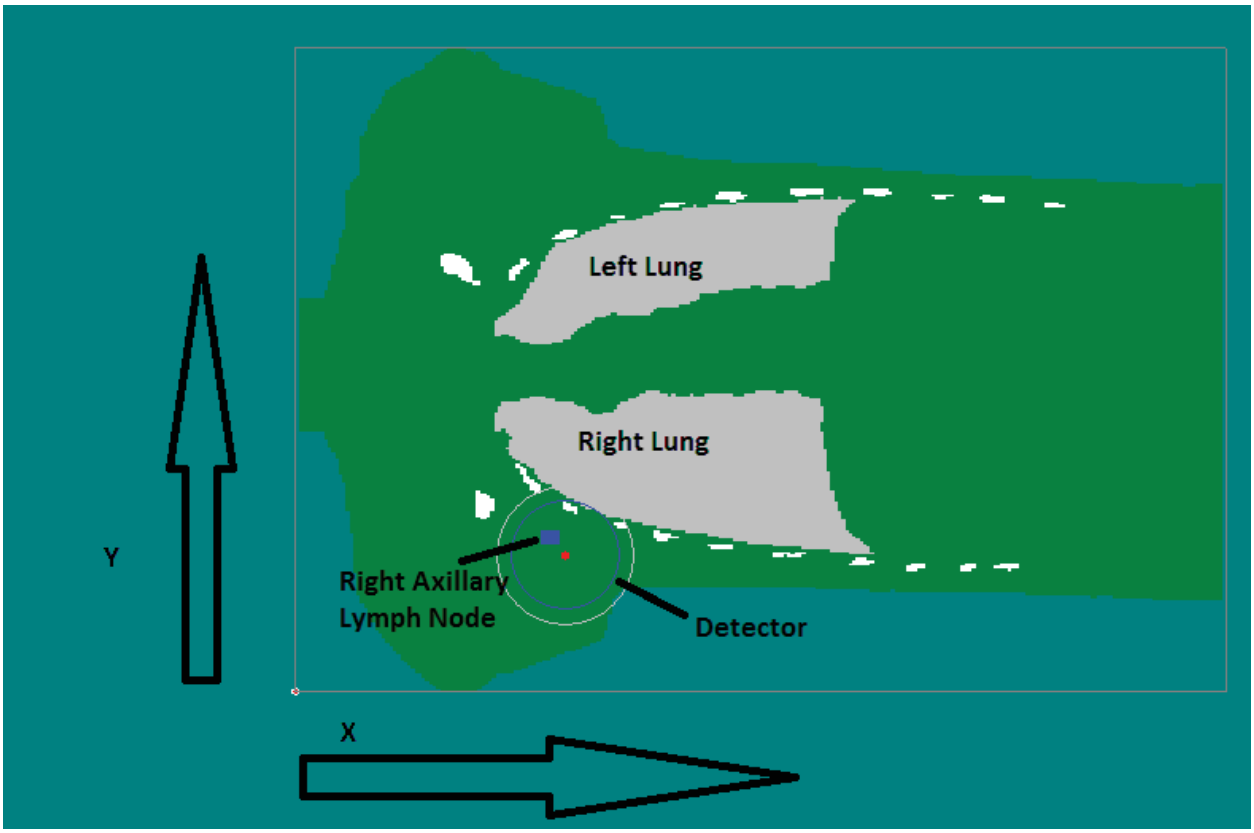

Figure 14. One vertical slice from VMC simulation illustrating the simulation of the LLNL torso phantom including the axillary lymph nodes.

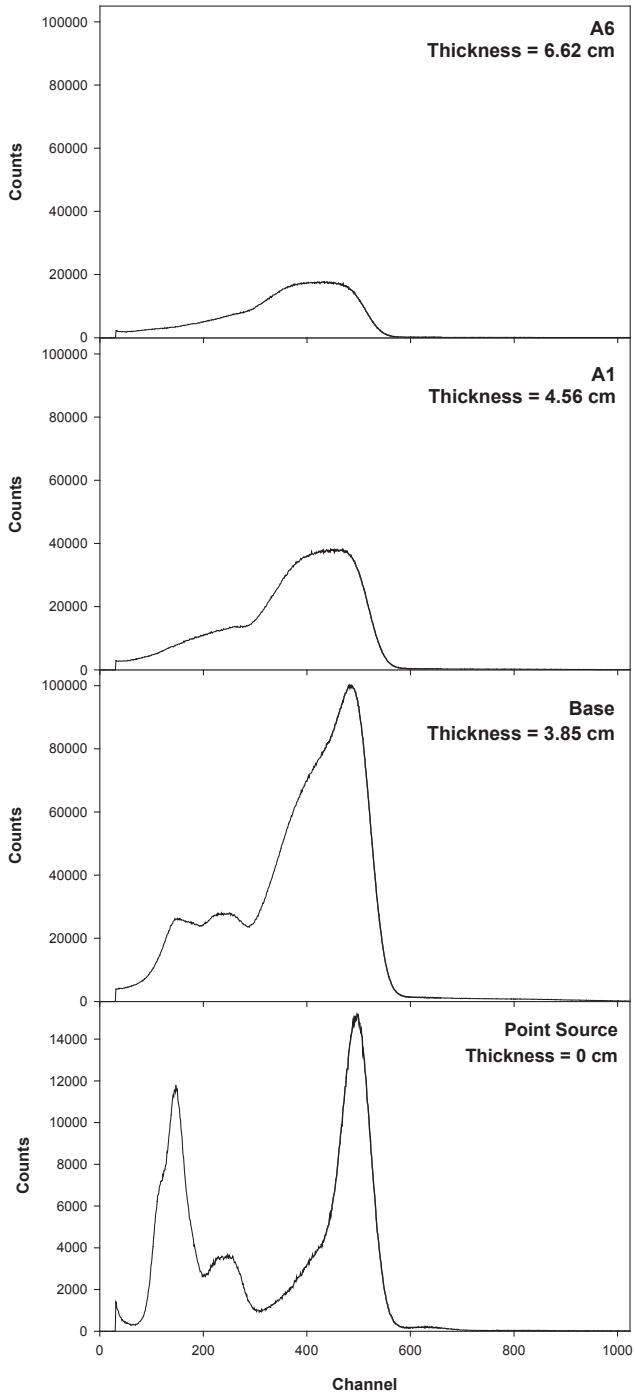

Figure 15. Photon energy spectra at various attenuating thicknesses measured with a pair of 7.62 cm diameter NaI(Tl) detectors and ^{241}Am deposited in the axillary lymph nodes inserted in the Livermore thoracic phantom. The shaded area represents the region of interest adopted for efficiency calculation.

Tables

Table 1. Decay data for americium-241 (Browne 1986).

γ mode	γ (keV)	γ (%)
Np L_{α}	13.927	13
Np L_{β}	17.611	20.2
Np L_{γ}	20.997	5.2
γE1	26.3445	2.4
γE1	59.5364	35.7

Table 2. Thickness values for original 100% muscle equivalent material overlays (Robbins 2001).

Series Name	Average Thickness (cm)	Range of Values (cm)	Measured Thickness (cm)	σ Measured Thickness (cm)	Total Thickness (cm)	σ Total Thickness (cm)
Base	1.56	1.43-1.64	1.825	0.467	1.825	0.467
C301-1	0.54	0.54-0.91	0.617	0.092	2.442	0.476
C290-2	1.12	1.12-1.57	1.305	0.08	3.13	0.474
C301-3	1.72	1.71-1.98	1.782	0.08	3.607	0.474
C290-4	2.44	2.44-2.70	2.586	0.107	4.411	0.479

Table 3. Median thickness, range, and total tissue thickness (overlay plate plus base plate) for each new overlay plate.

Overlay Plate	Median Thickness (cm)		Range of Thickness Values (cm)		Total Thickness (cm)	
	Left LN	Right LN	Left LN	Right LN	Left LN	Right LN
Base					**3.00**	**3.90**
A-1	0.813	0.711	0.335-1.161	0.340-1.133	3.81	**4.61**
A-2	0.579	0.660	0.152-1.082	0.193-1.092	3.58	**4.56**
A-3	0.962	0.782	0.526-1.367	0.371-1.245	**3.96**	**4.68**
A-4	1.295	0.851	0.203-1.732	0.147-1.913	**4.30**	**4.75**
A-5	0.408	0.655	0.140-0.838	0.008-1.186	3.41	**4.56**
A-6	2.641	2.771	0.218-3.040	0.572-3.790	**5.64**	**6.67**
A-7	1.547	1.261	0.201-2.192	0.315-2.240	**4.55**	**5.16**

Table 4. Anthropometric phantoms used to determine the calibration equations which populate the calibration matrix.

Phantom	Date	Activity (Bq)
Axillary Lymph Nodes Total	8/5/2007	$7.31 \times 10^4 \pm 636$
Liver	4/4/1997	$3.19 \times 10^4 \pm 394$
Lungs Total	1/23/2000	$1.54 \times 10^3 \pm 13.4$
Thoracic Skeleton[2]	1/1/1981	3.39×10^3
Skull	11/1/1994	$5.93 \times 10^4 \pm 370$

[2] Am-241 activity information from Neton 1988; beginning date of DOE research reports assumed for certification date (Cohen et al. 1984).

Table 5. Anthropometric phantom used in the unknown measurement to demonstrate applicability of the calibration matrix.

Phantom	Certification Date	Certified Activity (Bq)
Lungs Total	8/16/2001	$9.78 \times 10^3 \pm 90.86$

Table 6. Specifications for the detectors used in the comparison of the axillary lymph nodes calibration measurements.

Name	Manufacturer	Model	Detector Material	Detector Area (mm^2)	Detector Thickness (mm)	Window Material
Paired NaI(Tl)	Bicron[3]	3XM.080/3A	NaI(Tl)	4560 9120 (pair)	2.032	Aluminum
Square Phoswich	Bicron	6X6XH.5CSI(NA)/ NAI(Tl)/SS-B-H	CsI(Na) NaI(Tl)	23226	38.1 12.7	Beryllium
Round NaI(Tl)	Harshaw[4]	20MBSH4M/5H-0-X	NaI(Tl)	12668	4	Beryllium
HPGe	Canberra[5]	GL2820R	HPGe	2800 5600 (pair)	20	Carbon Composite

[3] Bicron, Saint-Gobain Crystals,17900 Great Lakes Parkway, Hiram, OH 44234-9681.
[4] Harshaw, Saint-Gobain Crystals, 17900 Great Lakes Parkway, Hiram, OH 44234-9681.
[5] Canberra Industries, Inc., 800 Research Parkway, Meriden, CT 06450, U.S.A.

Table 7. Activity of ^{241}Am (Bq) contained in axillary lymph nodes phantoms.

Phantom Type	Phantom ID Number	Date	Activity (Bq)
Axillary Lymph Node	UCLN-01	1/23/2000	36,951.9 ± 455.1
Axillary Lymph Node	UCLN-02		36,108.3 ± 444
	Sum of Activity		73,060.2 ± 635.81
Right Lung	UCLL78Am	8/5/2007	824.38± 10.17
Left Lung	UCSL78Am		712.49 ± 8.79
	Sum of Activity		1,536.87 ± 13.44

Table 8. Results from the application of the matrix method.

Deposition Location	Calculated Activity (Bq)	L_c	MDA
Axillary Lymph Nodes	141.27±29.14	47.11	94.21
Skeleton	169.24±23.36	5.24	10.48
Lungs	$1.15x10^4±1.7x10^3$	18.83	37.67
Liver	293.22±106.85	56.09	112.18

Table 9. Calibration factors calculated with VMC and measured.

Detector Position	Activity Location	VMC Calibration Factor (CPS/Bq)	Measured Calibration Factor (CPS/Bq)
Right Axillary Lymph Nodes	Axillary Lymph Nodes	4.44E-03	1.29E-02
Right Axillary Lymph Nodes	Lungs	7.63E-04	3.07E-04
Lungs	Axillary Lymph Nodes	4.17E-04	2.56E-04

Table 10. Range of thicknesses (cm) used in determining the calibration equations for the matrix method.

Measurement geometry (target organ)		*Organ with radioactivity deposition (source organ)*			
		Axillary Lymph Nodes	**Skeleton**	**Lungs**	**Liver**
	Axillary Lymph Nodes	3.90 cm-6.67 cm	1.56 cm-4.00 cm	3.90 cm-5.16 cm	3.90 cm-5.16 cm
	Skull	-	-	-	-
	Lungs	1.56 cm-4.00 cm	1.56 cm-4.00 cm	1.56 cm-4.00 cm	1.56 cm-4.00 cm
	Liver	1.56 cm-4.00 cm	1.56 cm-4.00 cm	1.56 cm-4.00 cm	1.56 cm-4.00 cm

Publications

Lobaugh M, Spitz H, Glover S. Detection efficiency for measuring Am-241 in axillary lymph nodes using different types and sizes of detectors. Health Phys 103: 279-285; 2012. DOI: 10.1097/HP.0b013e31825aad4a

Planned submission to the Health Physics Journal: Lobaugh M, Spitz H, Glover S. A method to adjust in vivo measurement results of Am-241 in the lungs for interference caused by activity deposited in other organs.

Glassford E, Spitz H, Lobaugh M, Spitler G, Succop P, Rice C. Evaluation of residual uranium contamination in the dirt floor of an abandoned metal rolling mill. Health Phys 104:179-188; 2013. DOI:10.1097/HP.0b013e3182732c73

Schneider N, Lobaugh M, Tan Z, Sandwall P, Chen P, Glover S, Cui L, Murry M, Dong Z, Torgue J, and Spitz H. Biodistribution of ^{212}Pb conjugated trastuzumab in mice. J. Radioanal Nucl Chem 296:75-81; 2013. DOI 10.1007/s10967-012-2243-7

Chunlei L, Nguyen Q, Ryan P, LeMasters G, Spitz H, Lobaugh M, Glover S, Grinshpun S. School bus pollution and changes in the air quality at schools: a case study. J. Environ. Monit. 11:1037-1042; 2009. DOI:10.1039/b819458k

Zeman R, Lobaugh M, Spitz H, Glover S, Hickman D. A calibration phantom for direct, in vivo measurement of Am-241 in the axillary lymph nodes. Health Phys 97:219-227; 2009. DOI:10.1097/HP.0b013e3181abab16

Mitchell T, Sandwall P, Rolfes B, Lobaugh M, Bowen J, Elliston J, Glover S, Spitz H. Feasibility of using dendroanalysis of uranium as a biomarker for environmental contamination. J Radioanal Nucl Chem 227: 223-225; 2008. DOI:10.1007/s10967-008-0734-3

References

Anderson A, Kaifer R. Six-inch-square phoswich detector array for plutonium lung counting. In: Griffith R, ed. Hazards control department annual technology review. Livermore, CA: Lawrence Livermore National Laboratory; UCRL-50007-81; 1982: 25-28.

Bentel GC, Marks LB, Hardenbergh PH, Prosnitz LR. Variability of the depth of supraclavicular and axillary lymph nodes in patients with breast cancer: is a posterior axillary boost field necessary? Int J Radiat Oncol Biol Phys 47:755-758; 2000.

Bistline R, Watters R, Lebel J. A study of translocation dynamics of plutonium and americium from simulated puncture wounds in beagle dogs. Health Phys 22: 829-831; 1972.

Browne E, Firestone R. Americium-241. In: Shirley V, eds. Table of radioactive isotopes. United States of America: John Wiley and Sons; 1986: 241-2-241-3.

Canberra Industries. Technical specifications for detector model GL2820RS. Meridian, CT: Canberra Industries, Inc.; 2004.

Carbaugh E, Lynch T, Antonio C, Medina-Del Valle F. Twenty-four years of follow-up for a Hanford plutonium wound case. Health Phys 99: 483-494; 2010.

Cohen N, Laurer G, Neton J, Hickman D, Maiello M. In vivo measurements of bone-seeking radionuclides. New York: New York University Medical Center; Annual Report to the Department of Energy 1981-1984; DE-AS02-77EV-04326; 1984.

Cohen N, Spitz H, Wren M. Estimation of skeletal burden of “Bone-seeking” radionuclides in man from in vivo scintillation measurements of the head. Health Phys 33: 431-444; 1977.

Currie, L. Limits for qualitative detection and quantitative determination. Analytical Chemistry 40(3): 586-593; 1968.

Ekstrom LP, Firestone RB. WWW table of radioactive isotopes [database online]. Berkeley, CA: Lawrence Berkeley National Laboratory; 2009. Available at http://ie.lbl.gov/toi/. Accessed 27 August 2010.

Fisher S, Hickman D, Zeman R, Richards K. Am-241 activity in axillary lymph nodes. In: Proceedings of the 53rd Annual Conference on Biological, Analytical, and Environmental Radiochemistry. Jackson Hole, WY: Lawrence Livermore National Laboratory; UCRL-PRES-235766; 2007: 1-19.

Gomez L, Lebel J, Watters R. The effect of lymph node removal on PuO2 translocation. Health Phys 22: 833-836; 1972.

Griffith R. Polyurethane as a base for a family of tissue equivalent materials. In: Proceedings of the 5th International Congress of the International Radiation Protection Association. Fontenay-aux-Roses, France: IRPA; 1982: 165-168.

Griffith R, Dean P, Anderson A, Fisher J. Fabrication of a tissue-equivalent torso phantom for intercalibration of in-vivo transuranic-nuclide counting facilities. In: Advances in radiation protection monitoring. Proceedings of an International Atomic Energy Agency international symposium. Vienna: International Atomic Energy Agency; IAEA-SM-229/56; UCRL-80343; 1978: 493-504.

International Commission on Radiological Protection. A review of the radiosensitivity of the tissues in bone. Oxford: Pergamon Press; ICRP Publication 11. Ann ICRP 11 (1); 1967.

International Commission on Radiological Protection. Report on the Task Group on Reference Man. Oxford: Pergamon Press; ICRP Publication 23. Ann ICRP 23 (1); 1975.

International Commission on Radiological Protection. Basic anatomical and physiological data for use in radiological protection reference values. Oxford: Pergamon Press; ICRP Publication 89. Ann ICRP 32 (3/4); 2002.

International Commission on Radiological Protection. Basic anatomical and physiological data for use in radiological protection – the skeleton. Oxford: Pergamon Press; ICRP Publication 70; Ann ICRP 25 (2); 1995.

Jeffers K, Hickman D. Historical review of lung counting efficiencies for low energy photon emitters. Health Phys pending publication; LLNL-JRNL-606732; 2012.

Johnson L, Bull E, Lebel J, Watters R. Kinetics of lymph node activity accumulation from subcutaneous PuO2 implants. Health Phys 18: 416-418; 1970.

Kellar J. Fabrication of an Anthropomorphic Calibration Phantom for In Vivo Measurement of Eu-152 in the Skull. Cincinnati, OH: University of Cincinnati; 1995. Master's Project.

Knoll G. Radiation detection and measurement. New York: John Wiley & Sons; 2000.

Kramer G, Inn K. A summary of the proceedings of the workshop on standard phantoms for in vivo radioactivity measurement. Health Phys 61: 893-894; 1991.

Kramer G, Lee T, Chang S. Chest wall thickness measurements of the LLNL phantom for small area germanium detector counting. Health Phys 79: 203-206; 2000.

Lobaugh M, Spitz H, Glover S. Detection efficiency for measuring Am-241 in axillary lymph nodes using different types and sizes of detectors. Health Phys 103: 279-285; 2012. DOI: 10.1097/HP.0b013e31825aad4a

Lynch T, Kathren R, McInroy J. Macrodistribution of plutonium and americium in four human skeletons. J Radiol Prot 8: 67-76; 1988.

National Council on Radiation Protection and Measurements. Development of a biokinetic model for radionuclide-contaminated wounds and procedures for their assessment, dosimetry and treatment. Bethesda, MD: NCRP Publications; NCRP Report No. 156; 2007.

Neton J. A method for the in vivo measurement of americium-241 at long times post-exposure. New York: New York University; 1988. Dissertation.

Palmer H, Rieksts G, Icayan E. 1976 Hanford americium exposure incident: in vivo measurements. Health Phys 45: 893-910; 1983.

Robbins A. A new method for performing in vivo efficiency calibration measurements suitable for chestwall thicknesses in excess of 4 cm. Cincinnati: University of Cincinnati; 2001. Thesis.

Saint-Gobain Ceramics and Plastics, Inc. Technical specifications for detector model 3XM.080/3A. Newbury, OH: Saint-Gobain Crystals & Detectors; 2005.

Sharma R, Haridasan T, Surendran T. False indications of an actinide lung burden arising from a contaminated finger wound. Health Phys 73:820-825; 1997.

Snyder S, Traub R. The Livermore phantom history and supplementation. Health Phys 98: 459-465; 2010. DOI:10.1097/HP.0b013e3181c03cc4

Spitz H, Glover S, Liu N, Smith B, Hickman D, Kruchten D, Anderson L. Measurement of the attenuation coefficient for Livermore thoracic phantom lungs fabricated using contemporary materials. Health Phys 67:39-46; 1994.

Spitz H, Lodwick J. Design, fabrication, and evaluation of a new calibration phantom for in vivo measurement of bone seeking radionuclides. Radiat Protect Dosim 89:275-282; 2000.

Zeman R, Lobaugh M, Spitz H, Glover S, Hickman D. A calibration phantom for direct, in vivo measurement of Am-241 in the axillary lymph nodes. Health Phys 97:219-227; 2009. DOI:10.1097/HP.0b013e3181abab16

Appendix A. Cramer's Rule

Cramer's Rule of Determinants, while tedious, can be used to solve the system of four equations with four unknowns for the matrix efficiency calibration method:

$$\begin{bmatrix} a_{LN,LN}(y) & a_{LN,bone}(y) & a_{LN,lungs}(y) & a_{LN,liver}(y) \\ a_{bone,LN}(x) & a_{bone,bone}(x) & a_{bone,lungs}(x) & a_{bone,liver}(x) \\ a_{lungs,LN}(x) & a_{lungs,bone}(x) & a_{lungs,lungs}(x) & a_{lungs,liver}(x) \\ a_{liver,LN}(x) & a_{liver,bone}(x) & a_{liver,lungs}(x) & a_{liver,liver}(x) \end{bmatrix} \begin{bmatrix} Q_{LN} \\ Q_{bone} \\ Q_{lungs} \\ Q_{liver} \end{bmatrix} = \begin{bmatrix} cps_{LN} \\ cps_{skull} \\ cps_{lungs} \\ cps_{liver} \end{bmatrix}$$

where x represents muscle equivalent chest wall thickness and y represents the muscle equivalent tissue thickness over the axillary lymph nodes. Deriving the equations for Cramer's Rule was helpful in determining the propagated uncertainty and minimum detectable activity for this method, shown later in this section.

Once the attenuating tissue thicknesses are determined, the equation entries to the efficiency matrix will be reduced to person-specific calibration factors. Then the system of equations can be solved using Cramer's Rule of Determinants:

$$Q_{LN} = \frac{D_{LN}}{D}$$

$$Q_{bone} = \frac{D_{bone}}{D}$$

$$Q_{lungs} = \frac{D_{lungs}}{D}$$

$$Q_{liver} = \frac{D_{liver}}{D}$$

where D is the determinant of the person-specific efficiency matrix (using column and row numbers for indices to conserve space):

$$D = a_{11}a_{22}a_{33}a_{44} - a_{11}a_{22}a_{34}a_{43} - a_{11}a_{23}a_{32}a_{44} + a_{11}a_{23}a_{34}a_{42} + a_{11}a_{24}a_{32}a_{43} - a_{11}a_{24}a_{33}a_{42}$$
$$- a_{12}a_{21}a_{33}a_{44} + a_{12}a_{21}a_{34}a_{43} + a_{12}a_{23}a_{31}a_{44} - a_{12}a_{23}a_{34}a_{41} - a_{12}a_{24}a_{31}a_{43}$$
$$+ a_{12}a_{24}a_{33}a_{41} + a_{13}a_{21}a_{32}a_{44} - a_{13}a_{21}a_{34}a_{42} - a_{13}a_{22}a_{31}a_{44} + a_{13}a_{22}a_{34}a_{41}$$
$$+ a_{13}a_{24}a_{31}a_{42} - a_{13}a_{24}a_{32}a_{41} - a_{14}a_{21}a_{32}a_{43} + a_{14}a_{21}a_{33}a_{42} + a_{14}a_{22}a_{31}a_{43}$$
$$- a_{14}a_{22}a_{33}a_{41} - a_{14}a_{23}a_{31}a_{42} + a_{14}a_{23}a_{32}a_{41}$$

and where D_i is the determinant of the matrix which replaces column i in the efficiency matrix with the count rate (cps) measurement vector for the monitored person. For example, D_{LN} is the determinant of the following matrix:

$$\begin{bmatrix} cps_{LN} & a_{LN,bone}(x) & a_{LN,lungs}(x) & a_{LN,liver}(x) \\ cps_{skull} & a_{bone,bone}(x) & a_{bone,lungs}(x) & a_{bone,liver}(x) \\ cps_{lungs} & a_{lungs,bone}(x) & a_{lungs,lungs}(x) & a_{lungs,liver}(x) \\ cps_{liver} & a_{liver,bone}(x) & a_{liver,lungs}(x) & a_{liver,liver}(x) \end{bmatrix}$$

Then the determinants for the partial matrices, which incorporate the measurement count rate vector, are:

$$D_{LN} = cps_1a_{22}a_{33}a_{44} - cps_1a_{22}a_{34}a_{43} - cps_1a_{23}a_{32}a_{44} + cps_1a_{23}a_{34}a_{42} + cps_1a_{24}a_{32}a_{43}$$
$$- cps_1a_{24}a_{33}a_{42} - a_{12}cps_2a_{33}a_{44} + a_{12}cps_2a_{34}a_{43} + a_{12}a_{23}cps_3a_{44}$$
$$- a_{12}a_{23}a_{34}cps_4 - a_{12}a_{24}cps_3a_{43} + a_{12}a_{24}a_{33}cps_4 + a_{13}cps_2a_{32}a_{44}$$
$$- a_{13}cps_2a_{34}a_{42} - a_{13}a_{22}cps_3a_{44} + a_{13}a_{22}a_{34}cps_4 + a_{13}a_{24}cps_3a_{42}$$
$$- a_{13}a_{24}a_{32}cps_4 - a_{14}cps_2a_{32}a_{43} + a_{14}cps_2a_{33}a_{42} + a_{14}a_{22}cps_3a_{43}$$
$$- a_{14}a_{22}a_{33}cps_4 - a_{14}a_{23}cps_3a_{42} + a_{14}a_{23}a_{32}cps_4$$

$$D_{LN} = cps_1(a_{22}a_{33}a_{44} - a_{22}a_{34}a_{43} - a_{23}a_{32}a_{44} + a_{23}a_{34}a_{42} + a_{24}a_{32}a_{43} - a_{24}a_{33}a_{42})$$
$$+ cps_2(-a_{12}a_{33}a_{44} + a_{12}a_{34}a_{43} + a_{13}a_{32}a_{44} - a_{13}a_{34}a_{42} - a_{14}a_{32}a_{43} + a_{14}a_{33}a_{42})$$
$$+ cps_3(a_{12}a_{23}a_{44} - a_{12}a_{24}a_{43} - a_{13}a_{22}a_{44} + a_{13}a_{24}a_{42} + a_{14}a_{22}a_{43} - a_{14}a_{23}a_{42})$$
$$+ cps_4(-a_{12}a_{23}a_{34} + a_{12}a_{24}a_{33} + a_{13}a_{22}a_{34} - a_{13}a_{24}a_{32} - a_{14}a_{22}a_{33} + a_{14}a_{23}a_{32})$$

$$D_{bone} = a_{11}cps_2a_{33}a_{44} - a_{11}cps_2a_{34}a_{43} - a_{11}a_{23}cps_3a_{44} + a_{11}a_{23}a_{34}cps_4 + a_{11}a_{24}cps_3a_{43}$$
$$- a_{11}a_{24}a_{33}cps_4 - cps_1a_{21}a_{33}a_{44} + cps_1a_{21}a_{34}a_{43} + cps_1a_{23}a_{31}a_{44}$$
$$- cps_1a_{23}a_{34}a_{41} - cps_1a_{24}a_{31}a_{43} + cps_1a_{24}a_{33}a_{41} + a_{13}a_{21}cps_3a_{44}$$
$$- a_{13}a_{21}a_{34}cps_4 - a_{13}cps_2a_{31}a_{44} + a_{13}cps_2a_{34}a_{41} + a_{13}a_{24}a_{31}cps_4$$
$$- a_{13}a_{24}cps_3a_{41} - a_{14}a_{21}cps_3a_{43} + a_{14}a_{21}a_{33}cps_4 + a_{14}cps_2a_{31}a_{43}$$
$$- a_{14}cps_2a_{33}a_{41} - a_{14}a_{23}a_{31}cps_4 + a_{14}a_{23}cps_3a_{41}$$

$$D_{bone} = cps_1(-a_{21}a_{33}a_{44} + a_{21}a_{34}a_{43} + a_{23}a_{31}a_{44} - a_{23}a_{34}a_{41} - a_{24}a_{31}a_{43} + a_{24}a_{33}a_{41})$$
$$+ cps_2(a_{11}a_{33}a_{44} - a_{11}a_{34}a_{43} - a_{13}a_{31}a_{44} + a_{13}a_{34}a_{41} + a_{14}a_{31}a_{43} - a_{14}a_{33}a_{41})$$
$$+ cps_3(-a_{11}a_{23}a_{44} + a_{11}a_{24}a_{43} + a_{13}a_{21}a_{44} - a_{13}a_{24}a_{41} - a_{14}a_{21}a_{43} + a_{14}a_{23}a_{41})$$
$$+ cps_4(a_{11}a_{23}a_{34} - a_{11}a_{24}a_{33} - a_{13}a_{21}a_{34} + a_{13}a_{24}a_{31} + a_{14}a_{21}a_{33} - a_{14}a_{23}a_{31})$$

$$D_{lungs} = a_{11}a_{22}cps_3a_{44} - a_{11}a_{22}a_{34}cps_4 - a_{11}cps_2a_{32}a_{44} + a_{11}cps_2a_{34}a_{42} + a_{11}a_{24}a_{32}cps_4$$
$$- a_{11}a_{24}cps_3a_{42} - a_{12}a_{21}cps_3a_{44} + a_{12}a_{21}a_{34}cps_4 + a_{12}cps_2a_{31}a_{44}$$
$$- a_{12}cps_2a_{34}a_{41} - a_{12}a_{24}a_{31}cps_4 + a_{12}a_{24}cps_3a_{41} + cps_1a_{21}a_{32}a_{44}$$
$$- cps_1a_{21}a_{34}a_{42} - cps_1a_{22}a_{31}a_{44} + cps_1a_{22}a_{34}a_{41} + cps_1a_{24}a_{31}a_{42}$$
$$- cps_1a_{24}a_{32}a_{41} - a_{14}a_{21}a_{32}cps_4 + a_{14}a_{21}cps_3a_{42} + a_{14}a_{22}a_{31}cps_4$$
$$- a_{14}a_{22}cps_3a_{41} - a_{14}cps_2a_{31}a_{42} + a_{14}cps_2a_{32}a_{41}$$

$$D_{lungs} = cps_1(a_{21}a_{32}a_{44} - a_{21}a_{34}a_{42} - a_{22}a_{31}a_{44} + a_{22}a_{34}a_{41} + a_{24}a_{31}a_{42} - a_{24}a_{32}a_{41})$$
$$+ cps_2(-a_{11}a_{32}a_{44} + a_{11}a_{34}a_{42} + a_{12}a_{31}a_{44} - a_{12}a_{34}a_{41} - a_{14}a_{31}a_{42} + a_{14}a_{32}a_{41})$$
$$+ cps_3(a_{11}a_{22}a_{44} - a_{11}a_{24}a_{42} - a_{12}a_{21}a_{44} + a_{12}a_{24}a_{41} + a_{14}a_{21}a_{42} - a_{14}a_{22}a_{41})$$
$$+ cps_4(-a_{11}a_{22}a_{34} + a_{11}a_{24}a_{32} + a_{12}a_{21}a_{34} - a_{12}a_{24}a_{31} - a_{14}a_{21}a_{32} + a_{14}a_{22}a_{31})$$

$$D_{liver} = a_{11}a_{22}a_{33}cps_4 - a_{11}a_{22}cps_3a_{43} - a_{11}a_{23}a_{32}cps_4 + a_{11}a_{23}cps_3a_{42} + a_{11}cps_2a_{32}a_{43}$$
$$- a_{11}cps_2a_{33}a_{42} - a_{12}a_{21}a_{33}cps_4 + a_{12}a_{21}cps_3a_{43} + a_{12}a_{23}a_{31}cps_4$$
$$- a_{12}a_{23}cps_3a_{41} - a_{12}cps_2a_{31}a_{43} + a_{12}cps_2a_{33}a_{41} + a_{13}a_{21}a_{32}cps_4$$
$$- a_{13}a_{21}cps_3a_{42} - a_{13}a_{22}a_{31}cps_4 + a_{13}a_{22}cps_3a_{41} + a_{13}cps_2a_{31}a_{42}$$
$$- a_{13}cps_2a_{32}a_{41} - cps_1a_{21}a_{32}a_{43} + cps_1a_{21}a_{33}a_{42} + cps_1a_{22}a_{31}a_{43}$$
$$- cps_1a_{22}a_{33}a_{41} - cps_1a_{23}a_{31}a_{42} + cps_1a_{23}a_{32}a_{41}$$

$$D_{liver} = cps_1(-a_{21}a_{32}a_{43} + a_{21}a_{33}a_{42} + a_{22}a_{31}a_{43} - a_{22}a_{33}a_{41} - a_{23}a_{31}a_{42} + a_{23}a_{32}a_{41})$$
$$+ cps_2(a_{11}a_{32}a_{43} - a_{11}a_{33}a_{42} - a_{12}a_{31}a_{43} + a_{12}a_{33}a_{41} + a_{13}a_{31}a_{42} - a_{13}a_{32}a_{41})$$
$$+ cps_3(-a_{11}a_{22}a_{43} + a_{11}a_{23}a_{42} + a_{12}a_{21}a_{43} - a_{12}a_{23}a_{41} - a_{13}a_{21}a_{42} + a_{13}a_{22}a_{41})$$
$$+ cps_4(a_{11}a_{22}a_{33} - a_{11}a_{23}a_{32} - a_{12}a_{21}a_{33} + a_{12}a_{23}a_{31} + a_{13}a_{21}a_{32} - a_{13}a_{22}a_{31})$$

where cps_i is the net counts per second measured at the i^{th} location for the monitored person.

Uncertainty Propagation for the Calculated Activity

Since the measurement results (count rate vector) and matrix entries are independent the uncertainty for each calculated activity can be determined from the following general error propagation equation:

$$\sigma_u{}^2 = \left(\frac{\delta u}{\delta x}\right)^2 \sigma_x{}^2 + \left(\frac{\delta u}{\delta y}\right)^2 \sigma_y{}^2 + \left(\frac{\delta u}{\delta z}\right)^2 \sigma_z{}^2 + \cdots$$

For the division of two independent variables, as is the case for Cramer's Rule, this becomes:

$$u = \frac{x}{y} \; with \; \sigma_u{}^2 = \left(\frac{1}{y}\right)^2 \sigma_x{}^2 + \left(\frac{-x}{y^2}\right)^2 \sigma_y{}^2$$

Then the uncertainty for each calculated organ activity is:

$$\sigma_{Q_{LN}}{}^2 = \left(\frac{\sigma_{D_{LN}}}{D}\right)^2 + \left(\frac{-D_{LN} \times \sigma_D}{D^2}\right)^2$$

$$\sigma_{Q_{bone}}{}^2 = \left(\frac{\sigma_{D_{bone}}}{D}\right)^2 + \left(\frac{-D_{bone} \times \sigma_D}{D^2}\right)^2$$

$$\sigma_{Q_{lungs}}{}^2 = \left(\frac{\sigma_{D_{lungs}}}{D}\right)^2 + \left(\frac{-D_{lungs} \times \sigma_D}{D^2}\right)^2$$

$$\sigma_{Q_{liver}}{}^2 = \left(\frac{\sigma_{D_{liver}}}{D}\right)^2 + \left(\frac{-D_{liver} \times \sigma_D}{D^2}\right)^2$$

where σ_D is the propagated uncertainty for the determinant of the efficiency matrix and σ_{D_i} is the propagated uncertainty for each partial determinant. The uncertainty matrix for the efficiency calibration matrix is composed of the root mean square error (RMSE) for the linear regression model entries and the standard deviation for mean value entries:

$$\sigma_a = \begin{bmatrix} \sigma_{a_{11}} & \sigma_{a_{12}} & \sigma_{a_{13}} & \sigma_{a_{14}} \\ \sigma_{a_{21}} & \sigma_{a_{22}} & \sigma_{a_{23}} & \sigma_{a_{24}} \\ \sigma_{a_{31}} & \sigma_{a_{32}} & \sigma_{a_{33}} & \sigma_{a_{34}} \\ \sigma_{a_{41}} & \sigma_{a_{42}} & \sigma_{a_{43}} & \sigma_{a_{44}} \end{bmatrix}$$

The uncertainty for the determinant, used to solve the system of equations, can be calculated using the same general equation given above, by finding the partial derivative of the determinant algebra calculations for each entry of the matrix:

$$\sigma_D{}^2 = \left(\frac{\delta D}{\delta a_{11}}\right)^2 \sigma_{a_{11}}{}^2 + \left(\frac{\delta D}{\delta a_{12}}\right)^2 \sigma_{a_{12}}{}^2 + \left(\frac{\delta D}{\delta a_{13}}\right)^2 \sigma_{a_{13}}{}^2 + \left(\frac{\delta D}{\delta a_{14}}\right)^2 \sigma_{a_{14}}{}^2 + \cdots + \left(\frac{\delta D}{\delta a_{44}}\right)^2 \sigma_{a_{44}}{}^2$$

$$\begin{aligned}
\sigma_D{}^2 = {} & (a_{22}a_{33}a_{44} - a_{22}a_{34}a_{43} - a_{23}a_{32}a_{44} + a_{23}a_{34}a_{42} + a_{24}a_{32}a_{43} - a_{24}a_{33}a_{42})^2 \sigma_{a_{11}}{}^2 \\
& + (-a_{21}a_{33}a_{44} + a_{21}a_{34}a_{43} + a_{23}a_{31}a_{44} - a_{23}a_{34}a_{41} - a_{24}a_{31}a_{43} + a_{24}a_{33}a_{41})^2 \sigma_{a_{12}}{}^2 \\
& + (a_{21}a_{32}a_{44} - a_{21}a_{34}a_{42} - a_{22}a_{31}a_{44} + a_{22}a_{34}a_{41} + a_{24}a_{31}a_{42} - a_{24}a_{32}a_{41})^2 \sigma_{a_{13}}{}^2 \\
& + (-a_{21}a_{32}a_{43} + a_{21}a_{33}a_{42} + a_{22}a_{31}a_{43} - a_{22}a_{33}a_{41} - a_{23}a_{31}a_{42} + a_{23}a_{32}a_{41})^2 \sigma_{a_{14}}{}^2 \\
& + (-a_{12}a_{33}a_{44} + a_{12}a_{34}a_{43} + a_{13}a_{32}a_{44} - a_{13}a_{34}a_{42} - a_{14}a_{32}a_{43} + a_{14}a_{33}a_{42})^2 \sigma_{a_{21}}{}^2 \\
& + (a_{11}a_{33}a_{44} - a_{11}a_{34}a_{43} - a_{13}a_{31}a_{44} + a_{13}a_{34}a_{41} + a_{14}a_{31}a_{43} - a_{14}a_{33}a_{41})^2 \sigma_{a_{22}}{}^2 \\
& + (-a_{11}a_{32}a_{44} + a_{11}a_{34}a_{42} + a_{12}a_{31}a_{44} - a_{12}a_{34}a_{41} - a_{14}a_{31}a_{42} + a_{14}a_{32}a_{41})^2 \sigma_{a_{23}}{}^2 \\
& + (a_{11}a_{32}a_{43} - a_{11}a_{33}a_{42} - a_{12}a_{31}a_{43} + a_{12}a_{33}a_{41} + a_{13}a_{31}a_{42} - a_{13}a_{32}a_{41})^2 \sigma_{a_{24}}{}^2 \\
& + (a_{12}a_{23}a_{44} - a_{12}a_{24}a_{43} - a_{13}a_{22}a_{44} + a_{13}a_{24}a_{42} + a_{14}a_{22}a_{43} - a_{14}a_{23}a_{42})^2 \sigma_{a_{31}}{}^2 \\
& + (-a_{11}a_{23}a_{44} + a_{11}a_{24}a_{43} + a_{13}a_{21}a_{44} - a_{13}a_{24}a_{41} - a_{14}a_{21}a_{43} + a_{14}a_{23}a_{41})^2 \sigma_{a_{32}}{}^2 \\
& + (a_{11}a_{22}a_{44} - a_{11}a_{24}a_{42} - a_{12}a_{21}a_{44} + a_{12}a_{24}a_{41} + a_{14}a_{21}a_{42} - a_{14}a_{22}a_{41})^2 \sigma_{a_{33}}{}^2 \\
& + (-a_{11}a_{22}a_{43} + a_{11}a_{23}a_{42} + a_{12}a_{21}a_{43} - a_{12}a_{23}a_{41} - a_{13}a_{21}a_{42} + a_{13}a_{22}a_{41})^2 \sigma_{a_{34}}{}^2 \\
& + (-a_{12}a_{23}a_{34} + a_{12}a_{24}a_{33} + a_{13}a_{22}a_{34} - a_{13}a_{24}a_{32} - a_{14}a_{22}a_{33} + a_{14}a_{23}a_{32})^2 \sigma_{a_{41}}{}^2 \\
& + (a_{11}a_{23}a_{34} - a_{11}a_{24}a_{33} - a_{13}a_{21}a_{34} + a_{13}a_{24}a_{31} + a_{14}a_{21}a_{33} - a_{14}a_{23}a_{31})^2 \sigma_{a_{42}}{}^2 \\
& + (-a_{11}a_{22}a_{34} + a_{11}a_{24}a_{32} + a_{12}a_{21}a_{34} - a_{12}a_{24}a_{31} - a_{14}a_{21}a_{32} + a_{14}a_{22}a_{31})^2 \sigma_{a_{43}}{}^2 \\
& + (a_{11}a_{22}a_{33} - a_{11}a_{23}a_{32} - a_{12}a_{21}a_{33} + a_{12}a_{23}a_{31} + a_{13}a_{21}a_{32} - a_{13}a_{22}a_{31})^2 \sigma_{a_{44}}{}^2
\end{aligned}$$

Following the same approach, the uncertainties for the partial determinants can be calculated by substituting the correct entries with the count rate vector and the uncertainty of the count rate vector. Now the uncertainty for the calculated activity in each organ can be calculated for the Cramer's Rule calculation.

Critical Level and MDA Calculations

Critical level (L_c) calculations are dependent on the uncertainty of the background measurement (at the specific location) and the choice of alpha (the acceptable risk of making a Type I error): $L_c = k_\alpha \sigma_B \epsilon$, where ϵ is the efficiency calibration factor converting counts to activity, σ_B is the uncertainty of the background measurement, and k_α is 1.645 for alpha equal to 5%. For this matrix method approach, the critical level at each measurement location is dependent not only on the background count rate measured at that location, but also on the increased background from cross-talk when activity is located in other proximal organs. The efficiency calibration factor for this application is the efficiency matrix algebra. Therefore, the L_c for each measurement location can be calculated by:

$$L_c = k_\alpha \sqrt{\left(\frac{\sigma DBack_i}{D}\right)^2 + \left(\frac{-DBack_i * \sigma_D}{D}\right)^2}$$

Where D is the determinant of the person-specific matrix (see above), σD is the propagated uncertainty for the determinant of the person-specific matrix (see above), $DBack_i$ is the partial determinant when the background count rate vector is inserted column i and $\sigma DBack_i$ is the uncertainty of the partial determinant with the count rate vector in column i. This is approach again is using Cramer's Rule to solve a system of equations, but instead of using the unknown measurement count rate vector, it is using the background count rate vector for that measurement, defined as:

$$Back_{LN} = \begin{bmatrix} BckCPS_{LN} \\ CPS_{Bone} \\ CPS_{lungs} \\ CPS_{liver} \end{bmatrix}$$

$$Back_{bone} = \begin{bmatrix} CPS_{LN} \\ BckCPS_{bone} \\ CPS_{lungs} \\ CPS_{liver} \end{bmatrix}$$

$$Back_{lungs} = \begin{bmatrix} CPS_{LN} \\ CPS_{bone} \\ BckCPS_{lungs} \\ CPS_{liver} \end{bmatrix}$$

$$Back_{liver} = \begin{bmatrix} CPS_{LN} \\ CPS_{Bone} \\ CPS_{lungs} \\ BckCPS_{liver} \end{bmatrix}$$

Where CPS_i is the count rate at organ i and $BckCPS_i$ is the background count rate measured at organ i. These background count rate vectors are a combination of the measured background count rate at the geometry and the count rate from the other organs to account for the increase in background from activity deposited elsewhere in the body. Then the uncertainties for these background count rate vectors are:

$$\sigma Back_{LN} = \begin{bmatrix} \sigma BckCPS_{LN} \\ \sigma CPS_{Bone} \\ \sigma CPS_{lungs} \\ \sigma CPS_{liver} \end{bmatrix}$$

$$\sigma Back_{bone} = \begin{bmatrix} \sigma CPS_{LN} \\ \sigma BckCPS_{bone} \\ \sigma CPS_{lungs} \\ \sigma CPS_{liver} \end{bmatrix}$$

$$\sigma Back_{lungs} = \begin{bmatrix} \sigma CPS_{LN} \\ \sigma CPS_{bone} \\ \sigma BckCPS_{lungs} \\ \sigma CPS_{liver} \end{bmatrix}$$

$$\sigma Back_{liver} = \begin{bmatrix} \sigma CPS_{LN} \\ \sigma CPS_{Bone} \\ \sigma CPS_{lungs} \\ \sigma BckCPS_{liver} \end{bmatrix}$$

Where σCPS_i is the uncertainty for the unknown measurement at geometry i and $\sigma BckCPS_i$ is the uncertainty for the background measurement at geometry i. The partial determinant when the

background count rate vector is inserted in column i ($DBack_i$) and the uncertainty of the determinant calculated when the background count rate vector is inserted in column i ($\sigma DBack_i$) are calculated in the same fashion as described above for calculating the activity using Cramer's Rule. Once the critical level is calculated the minimum detectable activity (MDA) can then be estimated by doubling L_c (Currie 1967).

Appendix B. R-squared and Probability of the F-test Statistic Sum

Calculations for R-squared and F-statistic

$$R^2 = 1 - \frac{SSE}{SST}$$

$$F = \frac{MSM}{MSE} = \frac{\frac{SSM}{DFM}}{\frac{SSE}{DFE}} \; or \; F = \frac{\frac{R^2}{DFM}}{\frac{1-R^2}{DFE}}$$

SSE = sum of squares error

SST = sum of squares total

MSM = mean square for the model

MSE = mean square error

SSM= sum of squares model

DFM = degrees of freedom model

DFE = degrees of freedom error (number of observations minus the DFM)

Cumulative Distribution Function for the F-distribution

Cumulative distribution function for the F-distribution gives the probability the random variable X is less than or equal to x (Pr X ≤ x) for the calculated F-statistic.

$$F(x; d_1, d_2) = I_{\frac{d_1 x}{d_1 x + d_2}}\left(\frac{d_1}{2}, \frac{d_2}{2}\right)$$

Where d_1 is the degrees of freedom for the model, d_2 is the degrees of freedom error, and

$$I_x(a, b) = \sum_{j=a}^{a+b-1} \binom{a+b-1}{j} x^j (1-x)^{a+b-1-j}$$

$$F(x; d_1, d_2) = I_{\frac{d_1 x}{d_1 x + d_2}}\left(\frac{d_1}{2}, \frac{d_2}{2}\right) = \sum_{j=\frac{d_1}{2}}^{\frac{d_1}{2}+\frac{d_2}{2}-1} \binom{\frac{d_1}{2}+\frac{d_2}{2}-1}{j} \left(\frac{d_1 x}{d_1 x + d_2}\right)^j \left(1 - \frac{d_1 x}{d_1 x + d_2}\right)^{\frac{d_1}{2}+\frac{d_2}{2}-1-j}$$

Because there were only 5 observations (n) made to determine the lungs and liver geometry efficiency calibrations, there were 4 degrees of freedom total (n-1), which got apportioned as d_1=d_2=2. Therefore the cumulative distribution function is:

$$F(x; 2,2) = \sum_{j=\frac{2}{2}}^{\frac{2}{2}+\frac{2}{2}-1} \binom{\frac{2}{2}+\frac{2}{2}-1}{j} \left(\frac{2x}{2x+2}\right)^j \left(1 - \frac{2x}{2x+2}\right)^{\frac{2}{2}+\frac{2}{2}-1-j}$$

$$F(x; 2,2) = \sum_{j=1}^{1} \binom{1+1-1}{j} \left(\frac{2x}{2x+2}\right)^j \left(1 - \frac{2x}{2x+2}\right)^{1+1-1-j}$$

$$F(x; 2,2) = \sum_{j=1}^{1} \binom{1}{j} \left(\frac{2x}{2x+2}\right)^j \left(1 - \frac{2x}{2x+2}\right)^{1-j}$$

$$F(x; 2,2) = \binom{1}{1} \left(\frac{2x}{2x+2}\right)^1 \left(1 - \frac{2x}{2x+2}\right)^0$$

$$F(x; 2,2) = \left(\frac{1!}{1!\,(1-1)!}\right) \left(\frac{2x}{2x+2}\right)^1 (1)$$

$$F(x; 2,2) = (1) \left(\frac{2x}{2x+2}\right)^1 (1)$$

$$F(x; 2,2) = \frac{2x}{2x+2} = \frac{x}{x+1}$$

For the F-test, we want to know the probability that the random variable X is greater than the F-statistic (given as x):

$$1 - F(x; 2,2)$$

Using the above equation to look at the sum of R^2 and probabilities for the F-test equaling 1:

$$R^2 + 1 - F(x; 2,2) = 1$$

Substituting the final *F(x;2,2)* equation above:

$$R^2 + 1 - \frac{x}{x+1} = 1$$

$$R^2 = \frac{x}{x+1} \; or \; R^2 = \frac{F}{F+1}$$

where F is the calculated F-statistic. Therefore, the sum of the model R-square and the probability used in the F-test is equal to 1 when R-square is equal to the above equation in terms of the F-statistic.

Calculation of the F-statistic

Now it needs to be shown that for the particular cases presented in my dissertation the calculation of the F-statistic will result in the same equation.

Calculation for the F-statistic in terms of R-squared is:

$$F = \frac{\frac{R^2}{DFM}}{\frac{1-R^2}{DFE}}$$

Substituting the degrees of freedom for the model and degrees of freedom for the error into this equation; for the data discussed, these are both equal to 2:

$$F = \frac{\frac{R^2}{2}}{\frac{1-R^2}{2}}$$

$$F = \frac{\frac{R^2}{2}}{\frac{1-R^2}{2}}$$

$$F = \frac{2R^2}{2(1-R^2)}$$

$$F = \frac{R^2}{(1-R^2)}$$

$$F(1-R^2) = R^2$$

$$F - FR^2 = R^2$$

$$F = FR^2 + R^2$$

$$F = R^2(F + 1)$$

$$\frac{F}{F + 1} = R^2$$